LMC CLUMP MASS FUNCTION FROM THE ALMA ARCHIVE

An ALMA Archival Study of the Clump Mass Function in the Large Magellanic Cloud

By

Nathan Brunetti, B.Sc.

A Thesis

Submitted to the School of Graduate Studies

in the Partial Fulfilment of the Requirements

for the Degree

Master of Science

McMaster University

McMaster University MASTER OF SCIENCE (2017) Hamilton, Ontario
(Physics and Astronomy)

TITLE: An ALMA Archival Study of the Clump Mass Function in the Large Magellanic Cloud

AUTHOR: Nathan Brunetti, B.Sc. (University of Massachusetts Amherst)
SUPERVISOR: Dr. Christine D. Wilson

NUMBER OF PAGES: xii, 114

Abstract

This thesis presents 1.3 mm and 3.1 mm continuum maps of seven star forming regions within the Large Magellanic Cloud (LMC) as observed with the Atacama Large Millimeter/Submillimeter Array (ALMA). The data were taken as part of six projects retrieved from the ALMA public archive plus one project observed specifically for this work. We developed a technique to combine Band 3 and Band 6 maps to estimate dust-only emission corrected for free-free emission contamination. We also present an automated `clean` masking script, with a listing of the code, which we adapted and used for all of the imaging in this thesis. From these observations we identify 32 molecular clumps in the LMC and estimate their total mass from their dust emission. We derive a cumulative clump mass function ($N(\geq M) \propto M^{\alpha+1}$) and fit it with a double power law to find $\alpha_{\rm low} = -1.76^{+0.07}_{-0.1}$, $\alpha_{\rm high} = -3.3^{+0.3}_{-0.6}$, and a break mass of 2500^{+700}_{-300} $\mathrm{M}_\odot$. Comparing to the clump mass function derived by Indebetouw et al. (2013) from carbon monoxide spectral line emission for 30 Doradus-10 shows a consistent mass range of clumps between 205 $\mathrm{M}_\odot$ and 5740 $\mathrm{M}_\odot$ as well as consistency between their single power law fit and our low mass power law index. Also comparing to core and clump mass functions from several star forming regions in the Milky Way we find consistency between most of their high mass indices and our low mass index, which is where the clump mass ranges overlap.

Acknowledgments

I would like to thank my supervisor Dr. Christine Wilson for giving me the opportunity to work on some truly amazing data and science and for her guidance throughout this project. Your enthusiasm for digging into a scientific mystery and pulling it apart to see how things tick has inspired and motivated me tremendously. It has been a challenging but rewarding couple years and I can't wait for the next four. I would also like to thank the members of my committee, Dr. Alison Sills and Dr. William Harris, who made my committee meeting and defense scientifically exciting and dare I say, a tad fun.

Thank you to my friends and classmates who took me in when I came to a new country for the first time and made me feel like a part of their group right from the start. There would be so much missing from my experiences of grad school if it wasn't for the motivation, distractions, collaboration, and general support from you all.

Finally, thank you to my parents, my wife, and all of my family. Your love and support has pushed me so far and truly helped me to get where I am. And when I head home for a respite from my work your interest in my adventures in the Great North always rejuvenates me.

Contents

List of Figures

List of Tables

List of Abbreviations

30 Dor-10 30 Doradus-10.

ACA Atacama Compact Array.

ALMA Atacama Large Millimeter/Submillimeter Array.

ASTE Atacama Submillimetre Telescope Experiment.

BEMBB broken emissivity modified blackbody.

BLAST balloon-borne large aperture submillimeter telescope.

CASA Common Astronomy Software Applications.

CO carbon monoxide.

CRTF CASA region text file.

Dec. declination.

FoV field of view.

FWHM full width at half maximum.

G/D gas-to-dust.

GMC giant molecular cloud.

HPBW half power beam width.

IMF initial mass function.

ISM interstellar medium.

LMC Large Magellanic Cloud.

MS measurement set.

PI principal investigator.

R.A. right ascension.

RMS root-mean-square.

S/N signal-to-noise.

SED spectral energy distribution.

SPW spectral window.

WCS world coordinate system.

WLM Wolf-Lundmark-Melotte.

YSO young stellar object.

Chapter 1

Introduction

1.1 Core And Clump Mass Functions

Observations of star forming regions within the Milky Way have repeatedly shown molecular gas and dust arranged in filamentary structures within and around giant molecular clouds (GMCs) and with knots of higher density clumps and cores throughout. This ubiquity holds for high mass and low mass clouds (Reid & Wilson 2006a) as well as those with very active star formation and those absent of star formation (Arzoumanian et al. 2011). Searching the nearest galaxies beyond the Milky Way has begun to show the same picture (for the Large Magellanic Cloud in carbon monoxide (CO): Fukui et al. 2008; Wong et al. 2011). As these structures appear to accompany star formation wherever we look it is likely of some fundamental importance to characterize them so that we can understand their link to star formation and whether this organization of clouds into filaments and clumps is the same throughout the universe.

To understand these structures it helps to begin with a rough sketch of their

spatial properties and associations. GMCs span sizes of $\sim 10\,\mathrm{pc}$ to $100\,\mathrm{pc}$, masses from $\sim 10^5\,\mathrm{M}_\odot$ to $10^7\,\mathrm{M}_\odot$ (Fujii et al. 2014), and host the vast majority of star formation within galaxies. However, to understand the actual sites of clustered and individual star formation requires stepping down in size further to clumps and cores, respectively (Lada et al. 1991a,b; Lada 1992). The term molecular clump is commonly used to bridge the gap between core and GMC. They are observed with sizes from $\sim 1\,\mathrm{pc}$ to $10\,\mathrm{pc}$, masses up to around $10^4\,\mathrm{M}_\odot$ (Fujii et al. 2014), and can go on to form zero to many stars (star clusters). Molecular gas cores are typically defined as small ($\lesssim$0.1 pc, $\lesssim$200 $\mathrm{M}_\odot$) overdensities where it is expected only one or several stars will soon form (Reid & Wilson 2006a). Molecular gas filaments span a wide range of shapes, sizes ($\sim 3\,\mathrm{pc}$ to $\sim 10\,\mathrm{pc}$ and up to $\sim 250\,\mathrm{pc}$), masses ($\sim 1500\,\mathrm{M}_\odot$ to $\sim 10^5\,\mathrm{M}_\odot$), and linear mass densities ($\sim 50\,\mathrm{M}_\odot\,\mathrm{pc}^{-1}$ to $\sim 9000\,\mathrm{M}_\odot\,\mathrm{pc}^{-1}$) (Hill et al. 2012; Könyves et al. 2015; André et al. 2016; Wang et al. 2016). They exist threading throughout spiral arms with GMCs strung along them, within GMCs with clumps along them, and within clumps with cores along them.

Studies of star forming clouds have measured the mass distributions of these cores and clumps, known as mass functions. When plotted as the cumulative number of objects in a field versus mass these mass functions can be compared between different regions. To characterize the mass function, they are typically fit by a single power law

$$N(\geq M) \propto M^{\alpha+1} \tag{1.1}$$

(Netterfield et al. 2009; Könyves et al. 2015; Freeman et al. 2017), a piece-wise double power law (Johnstone et al. 2001; Motte et al. 2001; Reid & Wilson

2005, 2006b,a; Pattle et al. 2017), or a log-normal function

$$N(\geq M) \propto 1 - \mathrm{erf}\left[(\ln M - A_0)/(\sqrt{2}A_1)\right] \tag{1.2}$$

(Netterfield et al. 2009; Könyves et al. 2015; Reid & Wilson 2005, 2006b,a) based upon the shape exhibited for a particular region. These functional forms are motivated by the tendency for the mass functions to have a long tail at high masses combined with a flatter portion or turnover at low masses. Physical arguments for choosing some form of power law fit come from the ubiquity of turbulence in the interstellar medium (ISM) which should result in the turbulent cascade populating different size scales following a power law distribution. Log-normal forms are argued as the result of the various stochastic processes shaping the distribution of molecular gas in clouds in different ways leading to a central limit theorem outcome for that distribution.

It is also common to calculate differential mass functions of cores and clumps by counting the number of objects that fall within finite width bins of mass. The differential form is analytically related to the cumulative form by taking the derivative with respect to mass. Equation 1.1 becomes

$$\frac{dN}{dM} \propto M^{\alpha} \tag{1.3}$$

where α will be the same for both the cumulative and differential mass functions calculated from a collection of objects. For simplicity, all power law indices are reproduced here as cumulative mass function indices (i.e. Salpeter 1955, $\alpha = \mathbf{-1.35}$).

Dust continuum measurements of core and clump masses have been carried

out for a variety of regions in the Milky Way. Netterfield et al. (2009) observed 50 square degrees of the Galactic Plane in Vela with the balloon-borne large aperture submillimeter telescope (BLAST) and fit cold cores ($<$14 K) with a power law of -3.22 ± 0.14 and warmer cores with an index of -1.95 ± 0.05. Both single power law and log-normal fits were carried out but due to the fact that their lower mass limit was relatively large (2.5 $M_\odot$) the results were effectively the same over their mass range.

738 cores were extracted from Herschel Gould Belt Survey observations of Aquila by Könyves et al. (2015) in which they fit their mass function with an index of -2.33 ± 0.06. Above 1 $M_\odot$ they also fit both a single power law and a log-normal function but found no significant preference for either function. Below 1 $M_\odot$ there was strong statistical evidence for their mass function being of a log-normal form with a peak of $(0.45 \pm 0.20)\,M_\odot$. However, applying an age correction based on a correlation they saw between core mass and density (possibly indicating higher mass cores evolved more quickly) and fitting the mass function again resulted in an index of -2.0 ± 0.2.

Pattle et al. (2017) observed the Cepheus flare region which included four molecular clouds with SCUBA-2. These were L1147/L1158, L1174, L1251 and L1228 and when their mass functions were fitted the power law indices were -1.8 ± 0.2, -2.0 ± 0.2, -1.8 ± 0.1 and -2.3 ± 0.3, respectively. When instead considering all four clouds together they fit two separate power laws to the total mass range as they noted a break in the mass function between 0.3 $M_\odot$ and 0.5 $M_\odot$. The first power law spanned 0.08 $M_\odot$ to 0.3 $M_\odot$ with an index of -1.9 ± 0.1 and the second spanned 0.5 $M_\odot$ to 3.5 $M_\odot$ with an index of -2.6 ± 0.3.

In addition to comparing mass distributions between different regions, core

mass functions such as the ones described above have also been related to the stellar initial mass function (IMF) as their shapes are often quite similar. Chabrier (2003, 2005) showed the stellar IMF, as determined primarily by Galactic field star observations, follows the original Salpeter (1955) power law index of -2.35 ± 0.30 above $1\,M_\odot$ with a log-normal turnover at low masses peaking around $0.2\,M_\odot$. This mass distribution has been observed to be universal across environments such as the Galactic disk, young and globular star clusters, and the spheroid or stellar halo (Chabrier 2003, 2005; Krumholz 2014). As a similar power law slope has been predicted for both the stellar IMF and core mass functions (Chabrier & Hennebelle 2010; Guszejnov & Hopkins 2015) this observed similarity in slopes has led to the idea that there exists a star formation efficiency that is independent of mass acting to transform the core mass function to the IMF (Alves et al. 2007; André et al. 2010; Könyves et al. 2015).

At higher masses there has been interest in comparing the mass distributions of whole star clusters to the clump mass functions within their natal GMCs (Lada 1992). Lada & Lada (2003) compiled a list of 76 young star clusters still embedded within a GMC and from this derived a cluster mass function with power law index of -2. Cluster masses calculated were between $\sim$50 and $1000\,M_\odot$. Fall & Chandar (2012) compared the mass functions and age distributions of star clusters from six different galaxies to find they were all well fit by power laws with indices of $\sim -1.9 \pm 0.2$. Galaxies included were the Milky Way, Large Magellanic Cloud (LMC), Small Magellanic Cloud, M83, M51 and Antennae (NGC 4038/9).

A natural challenge exists in observing young star clusters which is dust obscuration hiding the youngest, and therefore most deeply embedded, clus-

ters. This hinders our ability to fully constrain the initial mass distribution of clusters as their stars are first born. Cluster formation simulations can step in to attempt to bridge the gap between starless molecular clumps and the first star clusters as they emerge from their natal molecular clouds. It is important to be aware though that these simulations are still working to correctly treat the effect of feedback on the gas. One approach has been to start by running a hydrodynamical simulation of the parent GMC and after about a free-fall time instantaneously remove all the gas and switch to an N-body simulation of the stars formed. Fujii & Portegies Zwart (2015) took this approach and measure mass function indices of -1.73 at 2 Myr and -1.67 at 10 Myr for a range of initial GMC masses from $4 \times 10^4\,\mathrm{M}_\odot$ to $5 \times 10^6\,\mathrm{M}_\odot$. Howard et al. (2017) aimed to simulate cluster formation with the inclusion of radiative feedback in their hydrodynamical simulations to study its impact on cluster forming efficiency. Starting from GMCs of similar masses as Fujii & Portegies Zwart (2015) they found close agreement between their simulated mass function power law index of -1.99 ± 0.14 and observed embedded clusters. This was after 5 Myr and for masses from $10\,\mathrm{M}_\odot$ to $2000\,\mathrm{M}_\odot$. For clusters $> 2000\,\mathrm{M}_\odot$ they fit a steeper power law of -3.8.

With the wealth of information gathered on the mass distributions of cores and clumps in the Milky Way there is a need to extend the observational repertoire to other galaxies. This provides new environments to test models against as well as larger samples to draw statistical conclusions from. Two of our nearest neighbors, the Magellanic Clouds, are now well within reach of radio observations of molecular and dust emission for studies of the clump mass function. For example, Indebetouw et al. (2013) derived a CO mass function of 103 clumps at 0.46 pc resolution with the Atacama Large Millimeter/Submillime-

ter Array (ALMA). While extending beyond the Magellanic Clouds promises further variety of environments and larger sample sizes this pushes even the most advanced observatories to their limits. Rubio et al. (2015) reported on 10 CO clouds in the Wolf-Lundmark-Melotte (WLM) galaxy with masses of $5900\,M_\odot$ to $7.3 \times 10^4\,M_\odot$. At 1 Mpc distant and observed with ALMA they achieved $\sim$5 pc resolution. More recently, Schruba et al. (2017) observed NGC 6822 with ALMA reaching 2 pc resolution at a distance of 470 kpc. 156 CO clumps were extracted with masses of $9\,M_\odot$ to $3500\,M_\odot$. This shows that if we wish to sample the full range of clump sizes and possibly start to probe molecular core scales we are limited to the nearest Local Group members.

1.2 Large Magellanic Cloud

The LMC is a satellite dwarf galaxy gravitationally bound to the Milky Way. At a distance of (49.97 ± 1.11) kpc (Pietrzyński et al. 2013) it is the closest star forming galaxy (Wong et al. 2017) and contains the nearest super star cluster, R136 (Hunter et al. 1995; Massey & Hunter 1998). Its total mass, enclosed in a radius of 8.9 kpc, is $(8.7 \pm 4.3) \times 10^9\,M_\odot$ (van der Marel et al. 2002) which is broken into $2.7 \times 10^9\,M_\odot$ in stars (van der Marel et al. 2002), $(4.00 \pm 0.04) \times 10^8\,M_\odot$ in total gas (Roman-Duval et al. 2017) and the remainder in a dark halo.

Given its proximity the LMC is the ideal next step in studying star formation after our Galaxy. However, it is far more distant than any Milky Way clouds that can be used for comparison. This not only means we will be working with poorer physical scale resolution but we will also be biased towards brighter objects. Working with ALMA observations as in this thesis offers the

best counter to the issue of resolution we can currently achieve in the millimeter part of the spectrum, but we will still be limited to relatively larger star forming components than appear in most Milky Way studies. ALMA's sensitivity also helps to combat the bias towards only picking out the brightest sources but it cannot eliminate the issue. This is where careful characterization of the data is necessary (e.g. completeness estimation) to realistically limit our analysis to objects that should be well sampled by the observations.

The distance to the LMC not only allows for resolved observations of star forming clumps within GMCs but it is also a significantly different system from the Milky Way in which to study how stars form. Simply being a satellite galaxy that is interacting with the much larger Milky Way and another dwarf galaxy (the Small Magellanic Cloud and the Magellanic Bridge) creates a different environment to the Milky Way. The smaller gravitational potential changes the role star formation has through stellar feedback and supernovae in the evolution of the galaxy as a whole and thus on later generations of star formation. On top of this, a lower average metallicity of $\sim$1/3 – 1/4 $Z_\odot$ (Rolleston et al. 2002; Dufour 1984) introduces yet more variation from our Galaxy. Lower metal abundance results in smaller quantities of dust and thus less material to shield star forming regions from the background UV radiation field. This means molecular gas reservoirs may be smaller in mass (Fukui et al. 1999, 2001), limiting the star forming fuel throughout the galaxy. Fewer metals also reduces the cooling through line emission which can change the energy balance in molecular clouds. Finally, the characteristic peak mass of the stellar IMF has been predicted to shift to higher masses for low metallicity (Bromm 2005) (albeit for near-zero metallicity conditions).

We are also fortunate that from our vantage point the disk of the LMC

appears nearly face on. This simplifies the line-of-sight to regions of interest as we are observing the galaxy along its thinnest dimension. Also, uncertainties introduced by assuming common distances to objects across the LMC will be relatively small given this orientation as the degeneracy of near-side versus far-side is a relatively small difference. van der Marel et al. (2002) find a radially varying scale height for the LMC disk when fitting the vertical density profile with the form $\mathrm{sech}^2(z/z_0)$ with z_0 =0.27 kpc at the LMC center rising to z_0 =1.5 kpc at a radius of 5.5 kpc.

As we push observations to more distant objects we increase the sample sizes and variety of sources we can use to test theories of star formation, but this is always built upon the detailed work done on nearby objects. However, we also need to investigate those differing environments to further sample the parameter space nature works in. So it is the combination of these detailed nearby studies and the more distant but more varied studies that allows us to fully understand the processes of star formation. Working with clouds in the LMC begins to bring those two regimes together with high resolution observations of an entirely new environment. While the differences between the Milky Way and LMC make for interesting possibilities for differences in star formation they are still systems behaving in similar enough ways that a comparison is still useful. Both have disky morphologies, are actively forming stars, exhibit star formation sties being spatially correlated with the location of molecular gas, and contain a mixture of dust within molecular gas where stars are forming.

1.2.1 Individual Fields Studied In This Thesis

The Tarantula Nebula, or 30 Doradus, is one of the most actively star forming regions in the LMC. It harbors the R136 star cluster which boasts stellar densities somewhere between 10^4 and $10^7\,M_\odot\,pc^{-3}$ (Selman & Melnick 2013). Multiple generations of star formation have occurred in 30 Doradus over the course of $\sim$20 Myr (De Marchi et al. 2011; Walborn & Blades 1987). 30 Doradus has been observed as part of several LMC-wide surveys targeting different emission sources. In CO, it has been observed with NANTEN in ^{12}CO (1-0) (Fukui et al. 2008) and with MOPRA in ^{12}CO and ^{13}CO (1-0) (Hughes et al. 2010; Wong et al. 2011). The HERITAGE Key Project survey (Meixner et al. 2013) observed it in dust emission along with the rest of the LMC.

Part of 30 Doradus and within 11 pc projected distance of R136 is the GMC 30 Doradus-10 (as designated by Johansson et al. 1998). Indebetouw et al. (2013) observed 30 Doradus-10 (30 Dor-10) with ALMA and reported on ^{12}CO and ^{13}CO (2-1) emission as well as 1.3 mm dust continuum at $\sim$1.9″ resolution. The dust map was used to derive a total H_2 mass for the GMC of $(6 \pm 1) \times 10^4\,M_\odot$. Clumps were also identified in their ^{12}CO and ^{13}CO cubes using a custom clump finding algorithm that incorporates the Rosolowsky & Leroy (2006) CPROPS algorithm and those clump regions were used to calculate individual H_2 masses from both the dust and the CO data. Indebetouw et al. (2013) calculated a CO derived mass function for their 103 clumps and fit it with a power law index of $\alpha = -1.9 \pm 0.2$.

N159 was originally identified by Henize (1956) as an HII region and has since been extensively studied. Noted as the strongest CO intensity cloud in the initial NANTEN LMC survey (Fukui et al. 2008), N159 was later re-

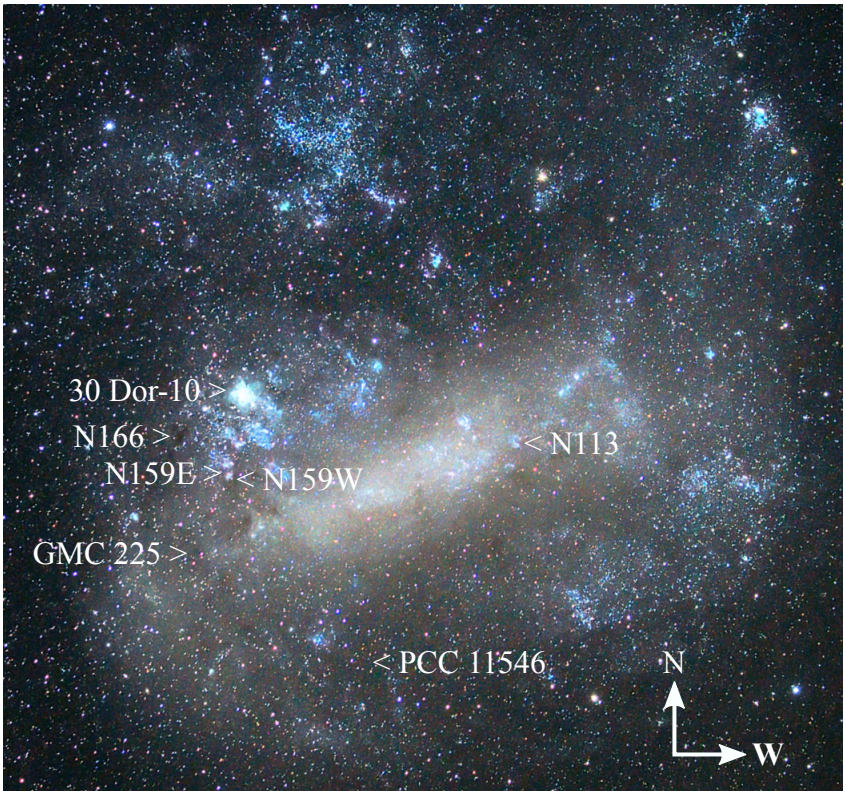

Figure 1.1: Approximate positions of the seven regions within the LMC observed with ALMA for the data used in this thesis. Background optical image credit: Primož Cigler (`http://astro.primozcigler.net`).

solved into three major clumps with NANTEN2 and Atacama Submillimetre Telescope Experiment (ASTE) observations designated N159E, N159W, and N159S (Mizuno et al. 2010). N159S does not exhibit any current star formation but the other two clumps do. ALMA observations of N159W appear to show that its constituent group of compact HII regions may have formed through a cloud-cloud collision (Fukui et al. 2015). By adding a dynamical estimate of one of the young stellar objects (YSOs) of 10^4 yr (using the first observed extragalactic protostellar outflows) Fukui et al. (2015) showed that the collisional triggering of star formation likely occurred very recently. N159E contains multiple developed HII regions, the most prominent of which is the Papillon Nebula (Mizuno et al. 2010). Saigo et al. (2017) suggested a three cloud collision is occurring in N159E , with the Papillon Nebula protostar in the overlap region. They also observe a molecular hole around the protostar filled with 98 GHz free-free emission indicating the protostar has recently begun disrupting the molecular cloud from which it formed.

N113 was also identified by Henize (1956) as an HII region. Subsequent observations have shown it contains the most intense maser in the Magellanic Clouds (Imai et al. 2013), clumpy molecular gas currently forming stars (Seale et al. 2012), a host of YSOs as identified by Herschel and Spitzer (Ward et al. 2016), and is related to three young stellar clusters (NGC 1874, NGC 1876, and NGC 1877; Bica et al. 1992). It also contains a rich assortment of molecular species as Paron et al. (2014) detected 8 molecular lines from 7 molecules towards N113 with ASTE.

N166 is yet another region originally identified by Henize (1956) and Fukui et al. (2008) also identified it as only containing HII regions with NANTEN. Two molecular clouds were observed overlapping its position in the second

NANTEN survey and a follow-up observation with ALMA targeted a position between those two NANTEN-observed clouds. N166 was also observed with ASTE in ^{12}CO (3-2) revealing densities of $10^2\,\mathrm{cm}^{-3}$ to $10^3\,\mathrm{cm}^{-3}$ and kinetic temperatures between 25 and 150 K in a 22″ beam (Paron et al. 2016).

GMC 225 is one of 272 GMCs identified by Fukui et al. (2008) in the second NANTEN survey of the LMC in ^{12}CO (1-0) and shows no signature of massive star formation (Kawamura et al. 2009, a Type I cloud in their designation). With a CO-derived total mass of $10^6\,\mathrm{M}_\odot$ and radius of ∼73 pc it was observed as part of a follow up ALMA project. It is ∼1500 pc south of 30 Dor-10 offset east from the molecular ridge.

PCC 11546 is an extremely cold ($\lesssim$15 K) dust source identified in the southern limits of the LMC as part of the Planck Galactic Cold Cloud catalog (Planck Collaboration et al. 2016). It has also been observed to exhibit strong CO (1-0) emission in the Planck integrated CO map and the MAGMA LMC CO survey (Wong et al. 2011). There appears to be a lack of massive star formation within PCC 11546 and it contains lower density gas than clouds closer to the center of the LMC (Wong et al. 2017).

The locations of these regions are marked in the optical image of the LMC in Figure 1.1.

1.3 Focus Of This Thesis

The investigation of environmental effects on the mass function of star forming cores and clumps requires more regions to be analyzed. Given the proximity of the LMC, observations of its star forming regions will address this need in the molecular clump regime. Measuring the dust emission of star forming clumps

offers a fairly straightforward method for determining total masses of clumps for deriving mass functions, and the sensitivity and high spatial resolution of ALMA are essential to sample the clump mass function adequately. Through the use of the public ALMA archive there is the possibility to build a sample of clumps throughout the LMC larger than can be accomplished through an individual proposal for observations. In this thesis, we undertook an ALMA archival search of star forming regions in the LMC that offer continuum dust observations and derived a composite clump mass function combining several different star forming clouds. We characterized our mass function with a double power law fit and compared our results to mass functions of Galactic star forming regions.

In Chapter 2 we summarize the observations from each ALMA project we used and we describe our continuum map making process. In Chapter 3 we describe our method of isolating the dust-only emission in each region, our clump identification procedure, and the steps we took to fit and characterize our final mass function. In Chapter 4 we discuss our results from Chapter 3 and place them into the broader context of the study of molecular clump mass functions. In Appendices, we provide a description of the automated `clean` masking script, along with a listing of the code itself, which we adapted and used for all of the imaging in this thesis.

Chapter 2

Observations And Data Reduction

2.1 Spectral And Spatial Setups

We retrieved six publicly available projects from the ALMA archive containing observations of seven fields in the LMC. These were the star forming regions 30 Dor-10, N159W, N159E, N113, N166, GMC 225 and PCC 11546. In addition, we submitted a proposal and received observations in Cycle 4 towards 30 Dor-10 with the 7 m Atacama Compact Array (ACA). This brings the total number of projects from which data is being presented here to seven. The projects were observed between December 31, 2011 and April 21, 2017 spanning Cycles 0 to 2 and 4. A summary of the observational details is given in Tables 2.1 and 2.2.

Table 2.1: Observational summary of fields.

Field Name	R.A. (J2000)	Dec. (J2000)	Project Code	Array[a]	Band[b]	No. Of Antennas[c]	Time On Source[d] (s)
30 Dor-10	05:38:48	-69:04:48	2011.0.00471.S	12	3	17	6757
”	”	”	”	”	6	18	6823
”	”	”	2016.1.01533.S	7	3	11	1198
”	”	”	”	”	6	12	15 484
N159W	05:39:37	-69:45:48	2012.1.00554.S	12	3	45	351
”	”	”	”	7	”	11	490
”	”	”	”	12	6	44	1357
”	”	”	”	7	”	7	1106
N159E	05:40:09	-69:44:44	”	12	3	26	312
”	”	”	”	7	”	11	1474
”	”	”	”	12	6	46	1533
”	”	”	”	7	”	11	1598

Continued on next page

[a] Identifies which sub-array of ALMA was used for observations in a given project, either the main array of 12 m dishes or the ACA of 7 m dishes.

[b] Observing Band 3 is centered near 95 GHz (3.1 mm) and Band 6 is centered near 225 GHz (1.3 mm).

[c] This is the total number of antennas that contributed data to the observations. However, this number does not take into account flagging of problematic antennas (e.g. software glitches, abormally high system temperatures, etc.) so fewer were likely used for actually producing the maps.

[d] Total time spent on each science target calculated from the observing scan times reported by the `listobs` Common Astronomy Software Applications (CASA) task.

Table 2.1: *continued*

Field Name	R.A. (J2000)	Dec. (J2000)	Project Code	Array[a]	Band[b]	No. Of Antennas[c]	Time On Source[d] (s)
N113	05:13:18	-69:22:25	2013.1.01136.S	12	6	44	1449
GMC 225	05:47:09	-70:40:16	2012.1.00603.S	”	3	27	791
”	”	”	”	7	”	12	2313
”	”	”	2013.1.01091.S	”	”	10	3379
”	”	”	”	12	6	35	842
”	”	”	”	7	”	9	1659
N166	05:44:29	-69:25:43	2012.1.00603.S	12	3	27	1456
”	”	”	”	7	”	12	4296
”	”	”	2013.1.01091.S	12	6	36	1696
”	”	”	”	7	”	10	2765
PCC 11546	05:24:09	-71:53:37	2013.1.00832.S	12	6	44	4508
”	”	”	”	7	”	10	4711

Table 2.2: Mapping summary of fields.

Field Name	Band	PI	Ref.[a]	Synthesized Beam[b] (″)	Largest Scales[c] (″)	Map Area[d] (Sq. ′)	No. Of Pointings[e]	Bandwidth[f] (GHz)
30 Dor-10	3	R. Indebetouw	1	2.17	55	2.5	10	4
”	6	”	”	1.51	22	1.2	30	”
N159W	3	Y. Fukui	2	2.50	49	2.4	17	1.9
”	6	”	”	1.25	22	1.6	65	1.6
N159E	3	”	3	2.56	49	1.8	19	1.9
”	6	”	”	1.10	22	1.8	61	1.6

Continued on next page

[a] First publication using these data: (1) Indebetouw et al. (2013); (2) Fukui et al. (2015); (3) Saigo et al. (2017); (4) Wong et al. (2017).

[b] As reported in the ALMA archive query tool. This is always taken from the 12 m array data.

[c] Maximum spatial scales the observations are sensitive to as set by the minimum baseline between dishes. Taken from 7 m array data except for N113.

[d] For regions of the mapped field above a gain response threshold of about 0.5 only. As these regions typically do not align with the R.A., Dec. directions, the area observed is smaller than the area from the dimensions in Table 2.4.

[e] Includes both 12 m and 7 m array pointings. All fields are mosaics except N113 which consisted of single pointing observations.

[f] Approximate bandwidth over which there is continuum data in the measurement sets (MSs) used to produce the final maps. This does not include gaps between sidebands or spectral windows (SPWs) where there are no data.

Table 2.2: *continued*

Field Name	Band	PI	Ref.[a]	Synthesized Beam[b] (″)	Largest Scales[c] (″)	Map Area[d] (Sq. ′)	No. Of Pointings[e]	Bandwidth[f] (GHz)
N113	”	C. Henkel	...	1.51	9	0.21	1	2.5
GMC 225	3	A. Kawamura	...	1.91	54	4.1	30	1.9
”	6	”	...	1.95	22	3.4	104	1.9
N166	3	”	...	3.44	49	7.1	44	1.9
”	6	”	...	1.62	22	4.0	170	1.9
PCC 11546	”	T. Wong	4	1.64	23	5.8	153	3.4

We were interested in measuring the dust masses in star forming regions; the projects we found contained data from 86 GHz to 100 GHz ($\sim$ 3.1 mm) and 217 GHz to 233 GHz ($\sim$ 1.3 mm) in ALMA's Bands 3 and 6, respectively. Band 7 observations ($\sim$ 350 GHz; $\sim$ 0.85 mm) were also present in the archive but there were almost no public observations of star forming regions in Band 7. While continuum emission observed in ALMA's Band 7 would would be near the peak of the blackbody emission from cold dust and thus isolate for the cold dust we had to instead use the less optimal Bands 3 and 6 because of public data availability. The lower frequencies of Bands 3 and 6 target a variety of molecular spectral lines at low and high redshift and continuum emission from cold dust but being farther down the Rayleigh-Jeans tail the contamination from other emission sources is significant.

We were most interested in the wide bandwidth continuum observations of these regions to attain high signal-to-noise (S/N) measurements of the thermal dust emission. There is also a multitude of spectral line data included in these projects but we do not use those data in this thesis. Effective bandwidths that we used in making continuum maps ranged between 1.6 GHz and 4 GHz.

For all but one region, multiple pointings were observed across each field in both bands to produce mosaic maps larger than the instantaneous field of view (FoV) of the array antennas. Mosaic pointings were roughly Nyquist-spaced in a given band to achieve relatively uniform coverage across the inner portion of the maps when imaged together. 12 m (main array) plus 7 m (ACA) data were obtained for all fields. The one exception was N113, which was observed as a single pointing and only with the 12 m array.

The pointings were mostly arranged in rectangular grids tilted at some position angle relative to the right ascension (R.A.) and declination (Dec.)

coordinate system (e.g. see Figure 2.1). Several sets of observations used a "flower petal" pattern (see Figure 2.2). Numbers of pointings on a field and in a single band range from 1 (N113) to 170 (N166) and are summarized in Table 2.2. Mapped areas cover between 0.21 square arcminutes (N113 in Band 6) and 7.1 square arcminutes (N166 in Band 3).

2.2 Calibration

To produce maps for each field and frequency, the raw interferometric visiblity data had to be retrieved from the archive, calibrated, and then imaged. The fundamental measurement of an interferometer, a visibility, is the amplitude and phase at a given time and frequency which describes the cross-correlated signal (interference pattern) between a single pair of antennas. All fields except 30 Dor-10 had only the lowest level raw data available in the archive. 30 Dor-10 had calibrated visibilities available and we used that data in our imaging. The raw data was either "manually" or pipeline calibrated at the observatory with the Common Astronomy Software Applications (CASA) package (McMullin et al. 2007). These calibrations are used for quality assurance before the data is released to the principal investigator (PI). The scripts to reproduce the observatory calibrated visibilities from the raw data are included in the archive.

Whenever the data had been manually calibrated at the observatory, we ran the full calibration procedure using the observatory scripts in the latest version of CASA available, 4.7.2-REL (r39762). Minor editing of the calibration scripts was usually necessary to account for task and parameter changes from the older versions of CASA.

Edits were also made to ensure the visibility weights were properly calcu-

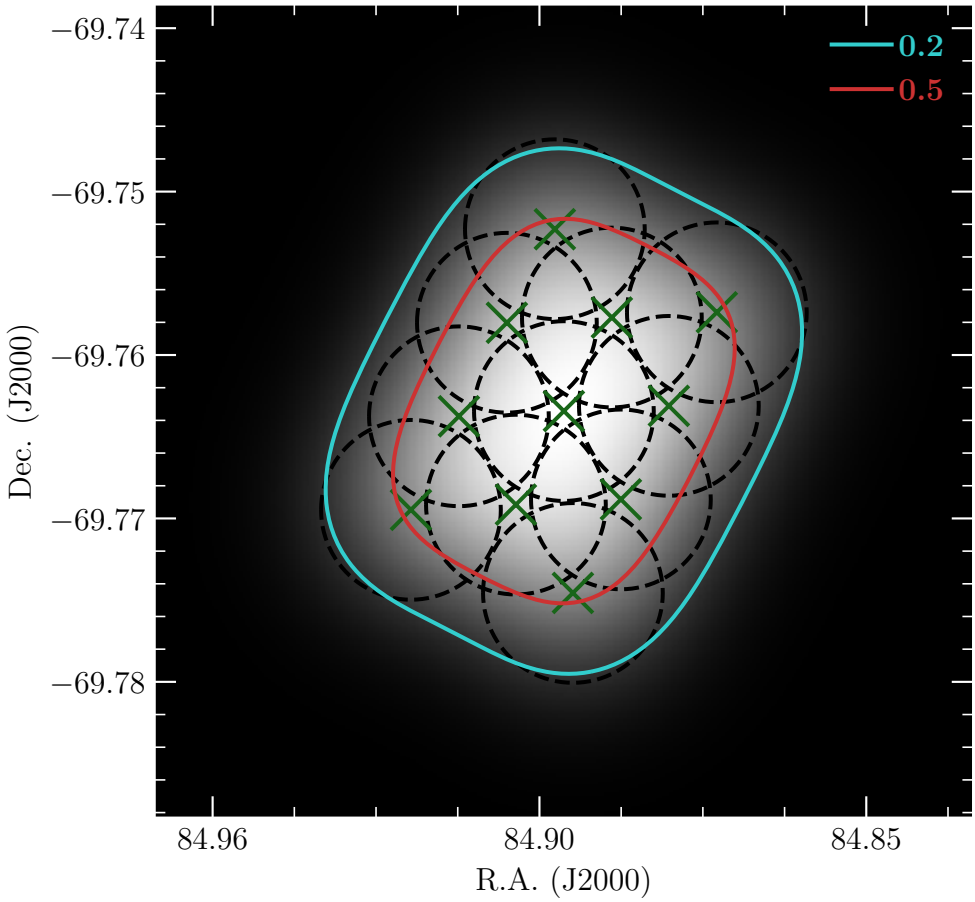

Figure 2.1: 7 m array coverage map of N159W in Band 6 showing a rectangular grid pointing pattern. Pointing centers are shown by green crosses, individual pointing half power beam widths (HPBWs) are shown as dashed black circles, the mosiaced coverage is shown in greyscale and blue and red contours mark the 20 % and 50 % gain response, respectively.

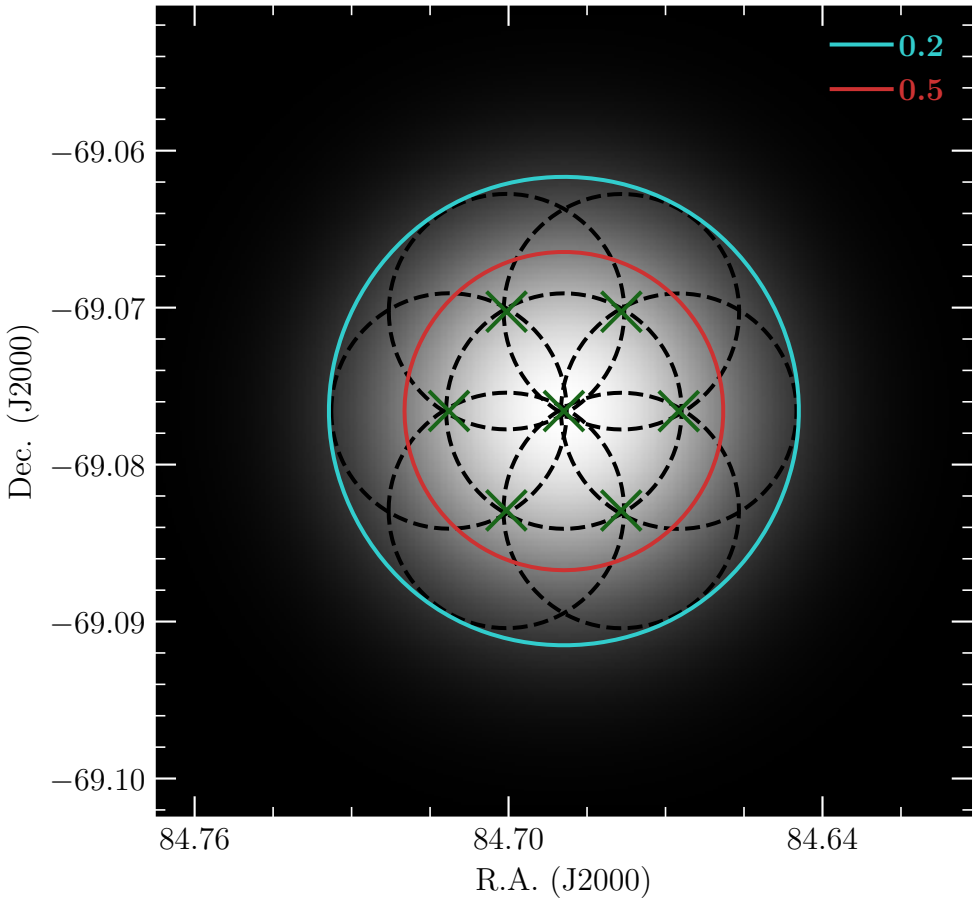

Figure 2.2: 12 m array coverage map of 30 Dor-10 in Band 3 showing a "flower petal" pointing pattern. Pointing centers are shown by green crosses, individual pointing HPBWs are shown as dashed black circles, the mosiaced coverage is shown in greyscale and blue and red contours mark 20 % and 50 % gain response, respectively.

lated throughout the entire calibration procedure. The procedure used was:

- ensure that all `applycal` calls were made with the `calwt=True` parameter setting (to properly calculate the visibility weights throughout calibration);
- any calls to `adjustweights` were commented out (as the weights should be properly handled with `calwt=True`);
- `standard='manual'` was specified in `setjy` calls that set the flux calibrator model amplitudes (a difference of CASA task syntax between versions); and
- `usescratch=True` was added to `setjy` calls to avoid invalid SOURCE_ID warnings.

Choosing to use the newest version of CASA for all manual calibrations meant we were working with the same version of the software across those data sets. A different version of the software was originally used for nearly every observation from our list of fields so this method was logistically simpler. It also made it simpler to make sure the weights were being calculated correctly across the various data sets. We were also able to take advantage of the more stable software and increased processing speeds that came with the more mature software. We carried out checks to verify the resultant calibrated data were reasonable and did not appear to suffer problems that might be due to using a newer version of CASA (discussed further below).

For data sets originally calibrated with the CASA pipeline at the observatory, the option to run a quick calibration restoration is available. Instead of running the entire calibration procedure again to derive the corrections and

flagging before applying them to the raw data, the final correction tables and flagging can be applied directly to the raw data to transform them into the final calibrated visibilities. This takes a fraction of the time to run and reproduces the same results as running the calibration procedure would. For pipeline calibrated data, we made sure to use the CASA and pipeline versions closest to those used by the observatory for the original calibration[1]. This is because the calibration pipeline has been undergoing extensive development over the last few years. In many cases this makes it practically impossible to make newer versions of the pipeline correctly handle the products of older versions without spending a prohibitively large amount of time massaging parameters and scripts and thoroughly checking the results to verify everything worked as expected. We found it easier to just acquire the pipeline versions needed and run each on the corresponding data. There was also no concern regarding data weights being improperly calculated due to older software, as all publicly available pipeline releases were after CASA 4.2.2 which contained a major correction to the handling of the weights.

Once calibrated data were obtained, either through the manual scripts or the pipeline restoration, we inspected the calibrated visibilities from the calibrator sources using the CASA `plotms` visibility plotter. This was done to ensure the results of the calibration were as expected (e.g. point source calibrators had constant amplitudes and zero phases across all baselines) and all seriously problematic data were flagged. Bandpass, phase, and flux calibrators had their amplitudes and phases vs. time and frequency checked across all antennas. In most cases this did not reveal that anything needed to be done

[1]All versions of CASA were downloaded from `https://casa.nrao.edu/casa_obtaining.shtml`.

Table 2.3: Details of data calibration.

Field	Array	Band	Calibration Method[a]	Restoration Version[b]
30 Dor-10	12	3 & 6	M	...
”	7	3	P	PL 38377 (C4-R2B), CASA 4.7.0-1 (r38335)
”	”	6	P	PL 39732 (C4-R2B), CASA 4.7.2 (r39762)
N159W	12	3 & 6	M	CASA 4.7.2 (r39762)
”	7	3	P	PL 34044 (C3-R1B), CASA 4.3.1 (r32491)
”	”	6	M	CASA 4.7.2 (r39762)
N159E	12	3	”	”
”	”	6	”	”
”	7	3 & 6	”	”
N113	12	6	P	PL 31667 (C2-R1B), CASA 4.2.2 (r30986)
N166	12	3 & 6	M	CASA 4.7.2 (r39762)
”	7	3	P	PL 31090 (C2-R1B), CASA 4.2.2 (r30986)
”	”	6	M	CASA 4.7.2 (r39762)
GMC 225	12	3	P	PL 31090 (C2-R1B), CASA 4.2.2 (r30986)
”	7[c]	3	P	PL 31090 (C2-R1B), CASA 4.2.2 (r30986)
”	7[d]	3	M	CASA 4.7.2 (r39762)
”	12 & 7	6	”	”
PCC 11546	12	”	”	”
”	7	”	”	”

[a] Indicates how the observatory did the original quality assurance calibration of the raw visibility data: with (M)anual scripts or with the CASA (P)ipeline.

[b] Indicates which version of CASA and the pipeline was used in this work to reproduce the observatory calibrated visibilities.

[c] From project 2012.1.00603.S.

[d] From project 2013.1.01091.S.

beyond the observatory-provided calibration process. A few cases, however, did expose situations where marginal antennas or edge channels should have been flagged and we did so before continuing to imaging. This also acted as a way to check that the calibration worked as expected when using a newer version of CASA than was originally used at the observatory.

Before the 30 Dor-10 visibilities were inspected we ran the CASA `clearcal` and `delmod` tasks on the calibrated measurement sets (MSs) that were retrieved directly from the ALMA archive (the MS is the CASA storage format that contains all of the visibilities and meta data for interferometric observations). This was to be certain that no additional calibration (i.e. self-calibration for imaging) was included in the MSs after the primary calibration. This also made certain no models were still stored in the MSs from imaging done at the observatory that could potentially interfere with our imaging steps.

To make continuum-only maps efficiently, we made a spectrally averaged MS containing all continuum-only data on a field for each band. As there were spectral lines present in all data sets, these channels needed to be flagged to image only the continuum emission. However, to properly image the continuum-only channels when spectral line channels had been flagged, we had to produce so-called channel-based weights, as opposed to weights only on the SPW level. This was done by copying the standard WEIGHT column into the WEIGHT_SPECTRUM column of each MS using the `initweights` CASA task. So for each band on each field we had to first initialize the channel-based weights, then flag spectral line channels, and finally average the continuum channels down to more manageable data sizes.

30 Dor-10 needed one extra step before even these steps could be carried out because the weights contained in the archival MSs had been calculated in

a CASA version before 4.2.2. This meant that the weights were not relatively correct between observations. To address this, we used the `statwt` CASA task to recalculate the 30 Dor-10 visibility weights empirically based on the scatter in the visibility data. This had to be done before the other steps because (1) we needed to know which channels contained spectral lines to avoid for the `statwt` recalculation and (2) proper weights needed to be in the WEIGHT column before they were copied to the WEIGHT_SPECTRUM column.

With the weights properly estimated for each field, channel-based weights initialized and the spectral line channels flagged, we made spectrally averaged data sets. Averaging was done such that all channels were no more than 125 MHz wide to avoid bandwidth smearing. For all fields that contained 12 m and 7 m data, the data were concatenated into a single, continuum-only, channel-averaged MS containing all the data on that field in that band.

2.3 Imaging

Since we intended to combine maps in the two bands to create a dust-only emission map for extracting clumpy sources, we wanted to match the spatial scales to which each pair of maps was sensitive as closely as possible. Appendix A gives a description of interferometric imaging and the `clean` algorithm for more context on the different beams and imaging weighting discussed here. Matching the spatial scale sensitivities was achieved through trimming the shortest spacings with the `uvrange` parameter in the CASA `clean` task and tapering the weighting of the longest spacings with the `outertaper` parameter, both done in the UV-plane. To choose the "inner" UV trimming to use (the minimum baseline length to include in imaging), we plotted the source

visibility amplitudes versus their radial UV lengths measured in wavelengths. The larger minimum baseline length between the two bands was identified and that number of wavelengths was used as the minimum baseline to include. For our fields, the larger minimum was always in the Band 6 data, so the `uvrange` trimming was always applied to the Band 3 data.

The "outer" UV tapering (the weighting applied to the maximum length baselines during imaging) directly changes the fitted synthesized beam that `clean` identifies and sets roughly the smallest spatial scales in the cleaned maps. We aimed to match the synthesized beam sizes exactly between the two bands through this tapering. Tapering can only decrease the resolution as it acts to down-weight long baseline visibilities. The Band 6 maps always had smaller synthesized beams before tapering than the Band 3 maps. Once the `uvrange` cut was made on the Band 3 data and a dirty map was made from it, we used the Band 3 synthesized beam as the target beam shape for the Band 6 maps. We preferred to use UV tapering to increase the size of the Band 6 synthesized beams as the initial beams were typically quite different between bands. A convolution, in the image plane, could have been performed on the Band 6 maps to match the resolutions. However, UV tapering works in the UV-plane before the data are Fourier transformed for cleaning in the image plane. We believe this method should more accurately match the spatial scale sensitives as cleaning is done only on data that includes the desired spatial frequencies.

Figure 2.3 shows the inner UV trimming for 30 Dor-10. Visibility amplitudes versus their baseline "distance" from a baseline of zero length are plotted as black points. The vertical orange dashed line shows the inner trimming made at 5091.93 λ. This number is taken from the Band 6 minimum baseline

and is applied to both bands in imaging, to be certain the minimum baselines match between bands. Figure 2.4 shows the two dimensional distribution of visibilities for 30 Dor-10 in black points and the "outer" UV tapering applied as the orange ellipse. The ellipse shows the Gaussian weighting profile full width at half maximum (FWHM) that was applied to match the synthesized beams between bands. We estimated the uvtaper that was required from the fact that the desired beam size (in arcseconds) is roughly equal to the uvtaper (in units of kilo-λ) divided by 200 kilo-λ. The vertical tapering may look extreme however it is not a hard cutoff but rather a Gaussian weighting that still includes contributions from data outside the ellipse.

Finding the outer tapering parameters to match the beams was not straightforward as we could not find a way to predict the tapering that was necessary to produce the synthesized beam we wanted. To overcome this, we used a simple trial-and-error approach. A first round of automated tapering tests were run using the CASA toolkit to quickly approximate the tapering effect on the UV data and to fit the synthesized beam. Tests were done with a grid of 2D Gaussian tapering major axes, minor axes and position angles. As the tapering in this technique was only approximate we then took our closest match and fine-tuned it using `clean` itself to produce dirty maps, until we matched the synthesized beam shapes reasonably well.

Matching the beam shapes exactly through tapering alone was practically impossible given the differences in intrinsic UV coverage between the observations. This is best illustrated by the difference in the UV data distributions for long baselines between Bands 3 and 6 for 30 Dor-10 shown in Figure 2.4. It manifests itself in not being able to very closely match the position angles of the beams between bands. To overcome this in the final step of cleaning,

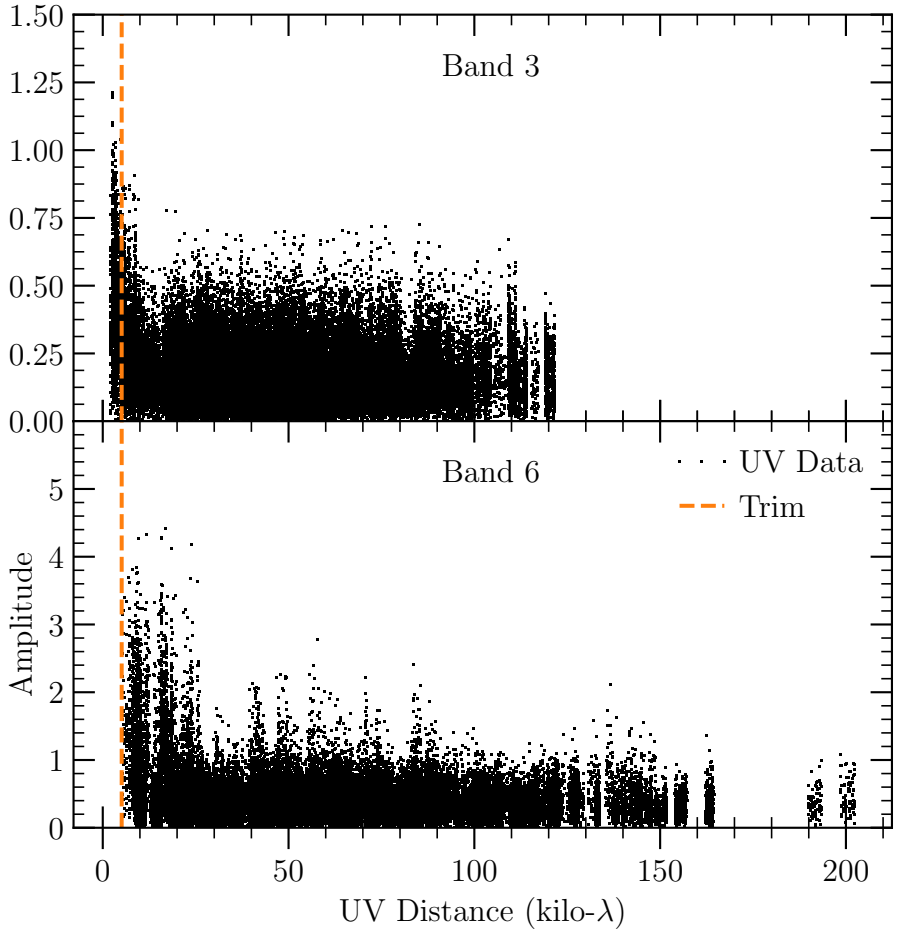

Figure 2.3: Interband UV trimming comparison for 30 Dor-10. The orange dashed line shows the "inner" UV trimming threshold applied to the Band 3 data. This is a strict cut so the location in the Band 3 distribution corresponds exactly to where the data begins in the Band 6 distribution.

the model map of point source pixels is convolved with the clean beam, which is by default a 2D Gaussian fit to the central portion of the dirty beam. The clean beam can be specified by the user, however, so that the desired Gaussian is convolved with the model map. We used this option to match the resolution of the cleaned emission between bands exactly. This was done by setting the `restoringbeam` parameter in `clean` to force the Band 6 Gaussian clean beam shape to be the same as for the Band 3 map. Note that this means all noise and any emission left in the residual maps is still at the tapered resolution and only the emission that was cleaned is exactly matched to the Band 3 resolution. Fortunately, we were always able to bring the beams into fairly close agreement even with just the tapering. Differences between Band 6 and Band 3 beam axes were $< 10\,\%$ (and usually much less) and position angles were $< 5\,\%$. 30 Dor-10 had a position angle difference between bands of $\sim 100\,\%$ which we could not match more closely. However, the difference was between position angles of $\sim 30^\circ$ and $\sim 60^\circ$ so the beam orientations were not terribly different.

At this point, the visibilities were ready to be imaged and cleaned in such a way as to match spatial scales between bands and so that the data weights were relatively correct between observations and arrays. We chose to clean all of the maps that showed obvious emission in their dirty maps, as they contained strong sources that caused the dirty beam sidelobes to contaminate the maps. There were fairly prominent negative bowls around these brighter sources as well that resulted, in part, from the dirty beam. An essential step in cleaning even moderately complex emission is in placing `clean` masks. These masks limit the `clean` algorithm to certain regions of the map for the cleaning process itself, and greatly improve the accuracy and speed of the process. This avoids

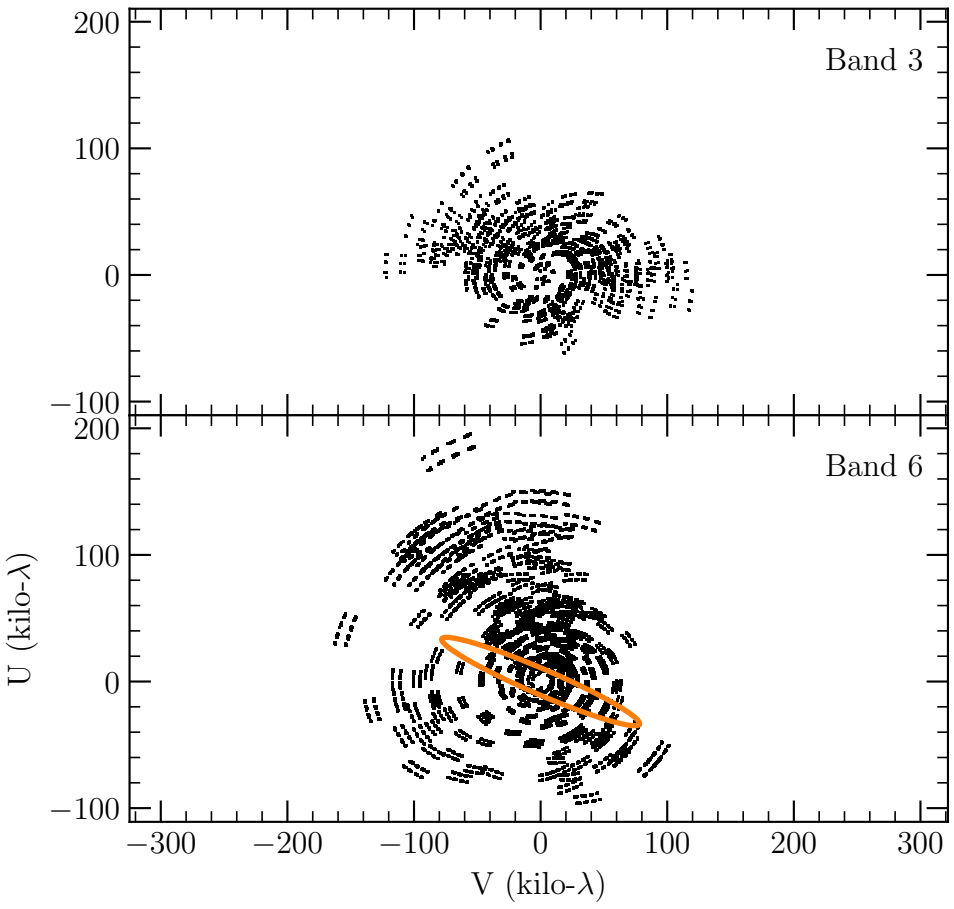

Figure 2.4: Interband UV-plane coverage comparison for 30 Dor-10. The orange ellipse marks the Gaussian tapering FWHM used to match the Band 6 synthesized beam to the Band 3 beam. While the tapering looks extreme in the vertical direction this is not a hard cutoff but a Gaussian weighting that will still include contributions from data outside the ellipse. It is also obvious that significant down-weighting in the vertical direction is needed as the Band 6 baseline distribution extends about twice as far as Band 3 in that direction.

erroneously picking out noise peaks and troughs along with negative bowls, causing "fake" emission to be "cleaned into" the map.

Motivated by the complexity of the emission in the 30 Dor-10 maps and by the desire to have a reproducible method of producing cleaned maps, we implemented an auto-masking algorithm for all cleaning. This algorithm is heavily based upon the auto-masking code given in the M100 CASA Guide as it appeared in August, 2016. We have modified it to work as an automated CASA script; when given a set of `clean` parameters, a minimum threshold to clean down to, a CASA region text file (CRTF) specifying an emission-free region of the dirty map, and a minimum spatial size to mask, the script iteratively cleans down to the desired threshold. See Appendix B for the details of how the auto-masking algorithm works, the steps we took to check the resulting maps, and a listing of the CASA script itself. All auto-masking was done with stopping thresholds between 1.5 and 3 times the map root-mean-square (RMS) and minimum mask areas of 0.5 times the map synthesized beam. All fields were cleaned with Briggs weighting (Briggs 1995)[2] (which uses the `robust` parameter described below), in multi-frequency synthesis mode, with `psfmode` set to psfclark and a maximum of 10^4 iterations. Table 2.4 lists the values used for common `clean` parameters for each field in all bands that were not the same across all fields.

[2]Also see Dan Briggs' PhD thesis at `http://www.aoc.nrao.edu/dissertations/dbriggs/` for the full details of the weighting scheme and for more information on the `robust` parameter discussed below.

Table 2.4: Unique `clean` parameter summary.

Field Name	Band	`cell` (″)	`imsize`[a] (pix)	`threshold` (μJy/bm)	`uvrange` (>λ)	`minpb`	`robust`	`outertaper` Major Axis (″)	`outertaper` Minor Axis (″)	`outertaper` Position Angle (°)
30 Dor-10	3	0.18	1152	300	5092	0.38	0.5	...	...	...
30 Dor-10	6	0.18	750	779	5092	0.38	0.5	0.85	0.1	67
N159W	3	0.213	1000	956	8023	0.4	0.5	...	...	...
N159W	6	0.213	720	1320	8023	0.4	0.5	2.76	1.64	81
N159E	3	0.21	1250	802	5956	0.5	0.5	...	...	...
N159E	6	0.21	750	1780	5956	0.5	0.5	3.05	1.45	−70
N113	”	0.13	”	396	...	0.5	0.5	...	...	...
GMC 225	3	0.32	700	...	...	0.5	2	...	...	...
GMC 225	6	0.11	1500	...	...	0.5	2	...	...	...
N166	3	0.38	1050	...	...	0.5	2	...	...	...
N166	6	0.155	1568	...	...	0.5	2	...	...	...
PCC 11546	”	0.126	1680 × 2400	...	...	0.5	2	...	...	...

NOTE.—Columns to the right of “Band” column are named after `clean` task parameter names.

[a] Entries with a single value report the length of all sides as maps were made square.

Cleaning was only performed on fields where there was clearly emission in the dirty maps made from those fields. This means that N166, GMC 225 and PCC 11546 were not cleaned. In these cases only dirty maps were made. From these maps we could measure the synthesized beams for comparison to the fields with detected emission along with the sensitivity achieved at that resolution. Also of note, since we only had access to Band 6 data for N113 there was no uvrange trimming or tapering done as there was no need to match spatial scales between bands.

We tried improving the S/N in the maps with no continuum emission by changing the imaging weighting for those maps. All imaging with `clean` was done with the `robust` parameter set to 0.5. This parameter can be varied to either increase the resolution of the map at the cost of higher noise or reduce the noise in the map while also decreasing the resolution (this is discussed further in Appendix A). With `robust=0.5` the output map is fairly balanced between resolution and noise (it can be set anywhere between -2.0 and 2.0). To try to extract any detection we could from the non-detection maps we set `robust=2.0` in `clean` to boost the S/N as much as possible. While the noise did drop, it was not enough to detect emission in any of the non-detection maps. The RMS noise and beam shapes listed in Table 2.5 for GMC 225, N166, and PCC 11546 refer to the maps made with `robust=2.0`.

For completeness, all steps described above, from inspecting the visibilities with `plotms` up to and including cleaning the maps, were carried out in CASA 4.7.2 (r39762) for all fields. All final Band 3 and Band 6 maps (either cleaned or not based on presence of continuum emission) are shown in Figures 2.5 to 2.10. The average synthesized beam size was $\sim 2.3''$ corresponding to ~ 0.6 pc at the distance to the LMC.

Table 2.5: Imaging summary of fields.

Field Name	Map Type	Major Axis (″)	Minor Axis (″)	Position Angle (°)	RMS Noise[b] (μJy/beam)
30 Dor-10	Dust	2.25	1.40	65	410
”	Band 3	”	”	”	150
”	Band 6	”	”	”	390
N159W	Dust	2.63	1.67	82	496
”	Band 3	”	”	”	637
”	Band 6	”	”	”	527
N159E	Dust	2.90	1.61	−77	662
”	Band 3	”	”	”	321
”	Band 6	”	”	”	595
N113	”	1.35	1.04	61	264
GMC 225[a]	Band 3	4.26	3.13	−67	182
”	Band 6	2.01	1.13	−86	760
N166[a]	Band 3	4.08	3.57	−73	196
”	Band 6	2.17	1.61	69	942
PCC 11546[a]	”	1.81	1.23	75	192

NOTE.—Synthesized beam shape parameters are given for the final images used to create our clump mass function.

[a] Fields with no emission detected show beam shapes and noise estimates from maps made with all 12 m and 7 m data and `robust=2` set in `clean`. This setting was used to maximize S/N but also results in a larger beam size when used.

[b] Noise measurements were made in emission-free regions of the dirty map for each field.

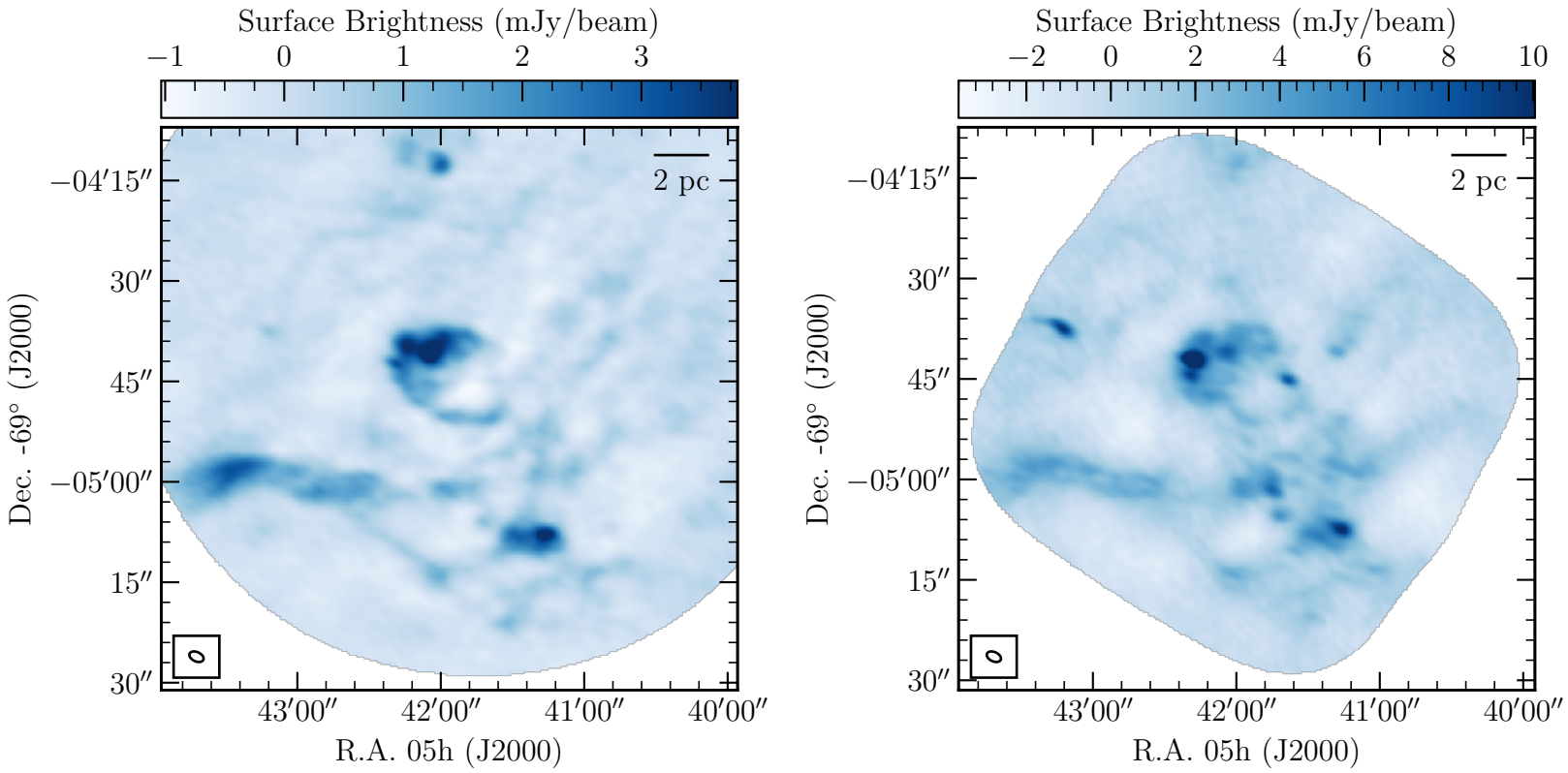

(a) Band 3

(b) Band 6

Figure 2.5: Cleaned and beam-matched continuum ALMA maps of 30 Dor-10.

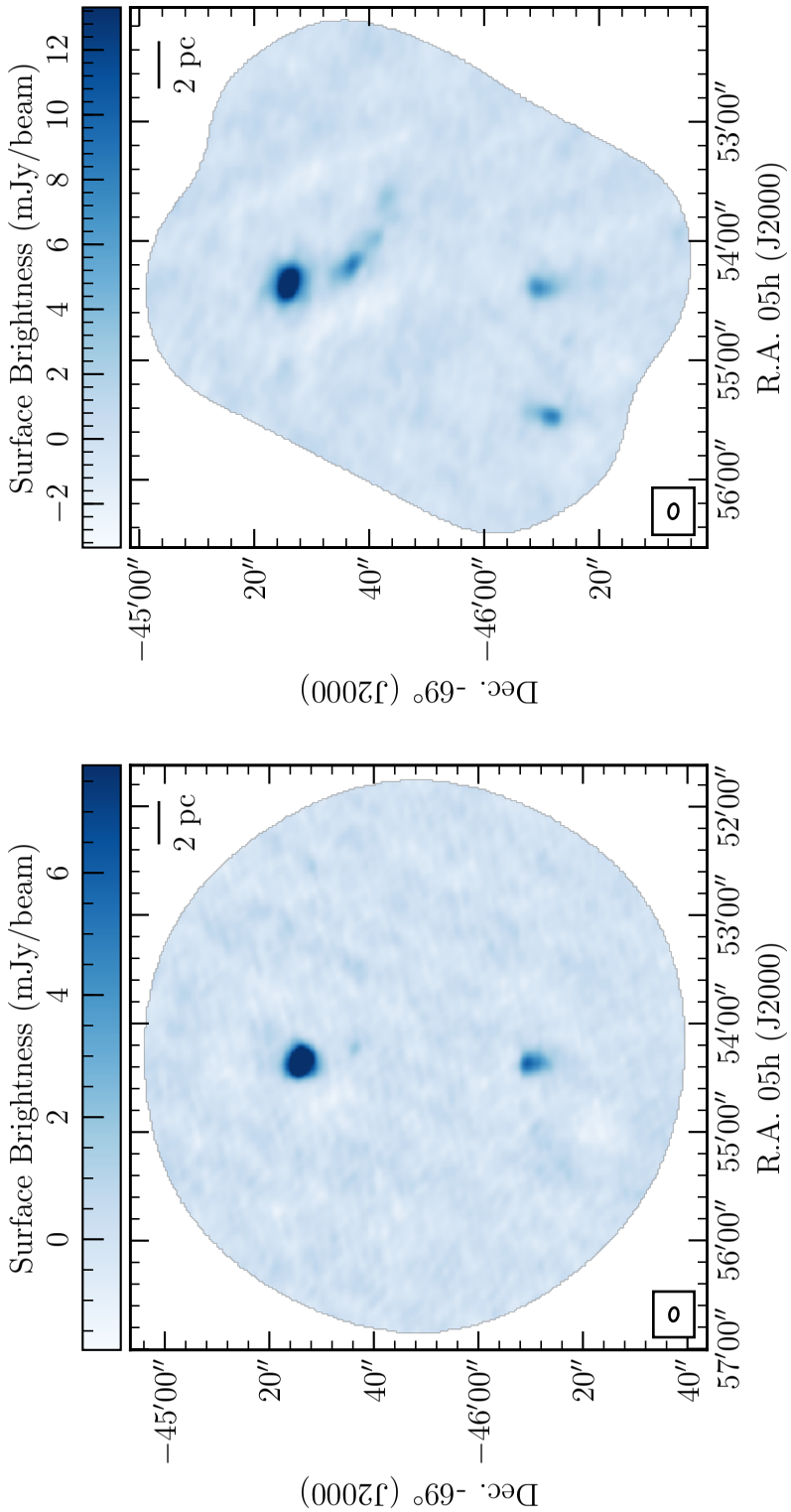

(a) Band 3

(b) Band 6

Figure 2.6: Cleaned and beam-matched ALMA continuum maps of N159W.

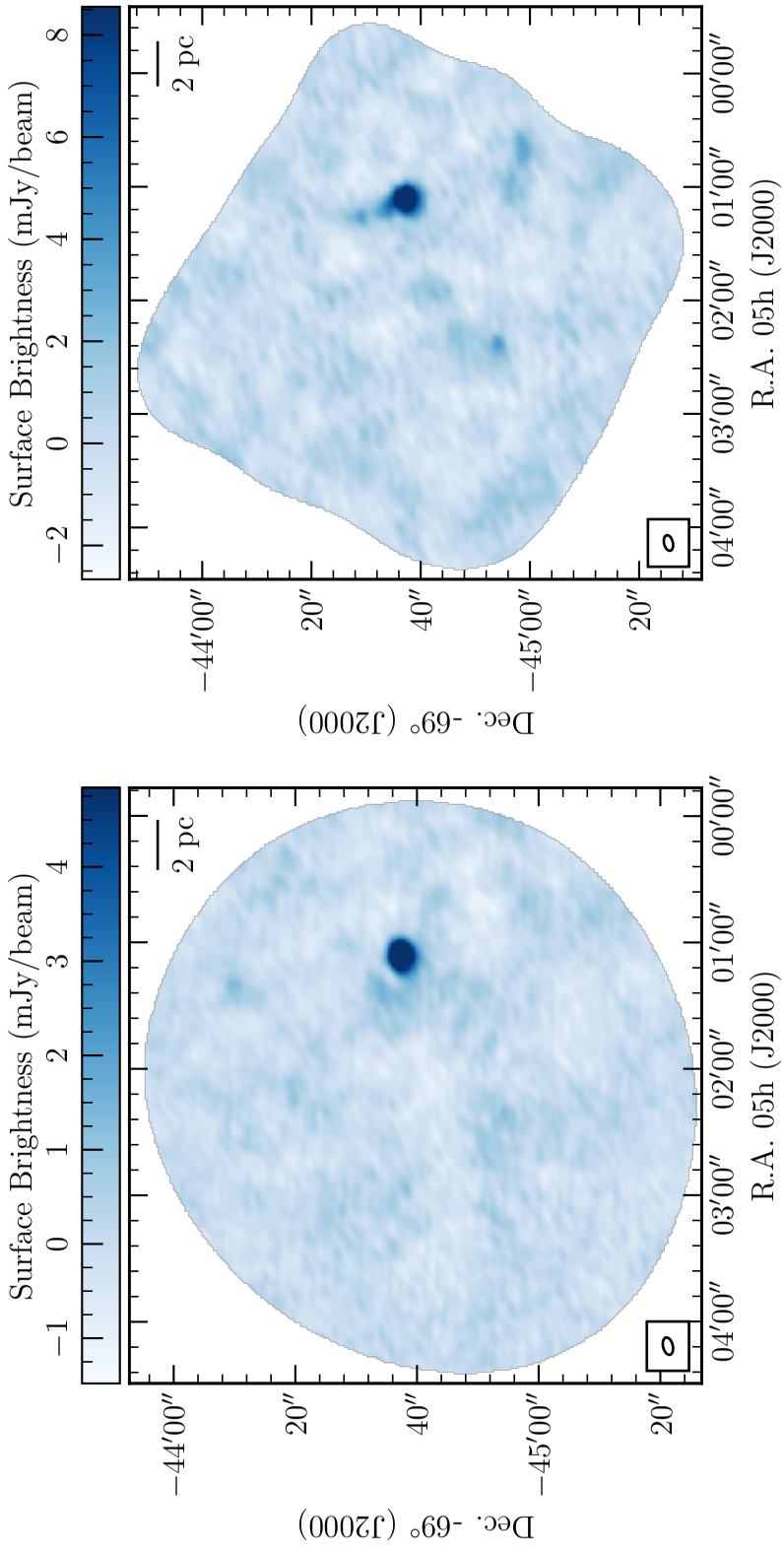

(a) Band 3

(b) Band 6

Figure 2.7: Cleaned and beam-matched ALMA continuum maps of N159E.

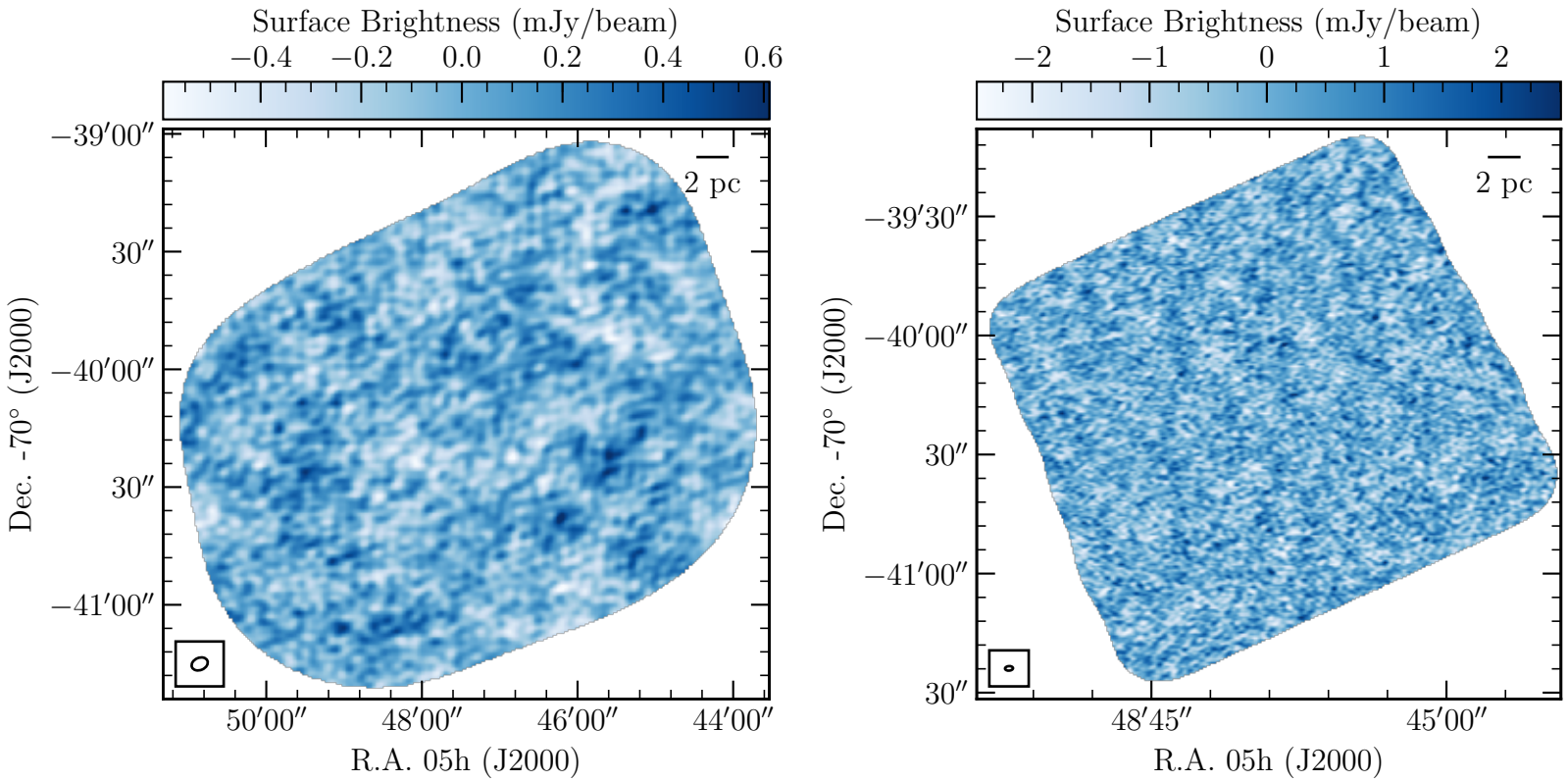

(a) Band 3

(b) Band 6

Figure 2.8: Dirty ALMA continuum maps of GMC 225.

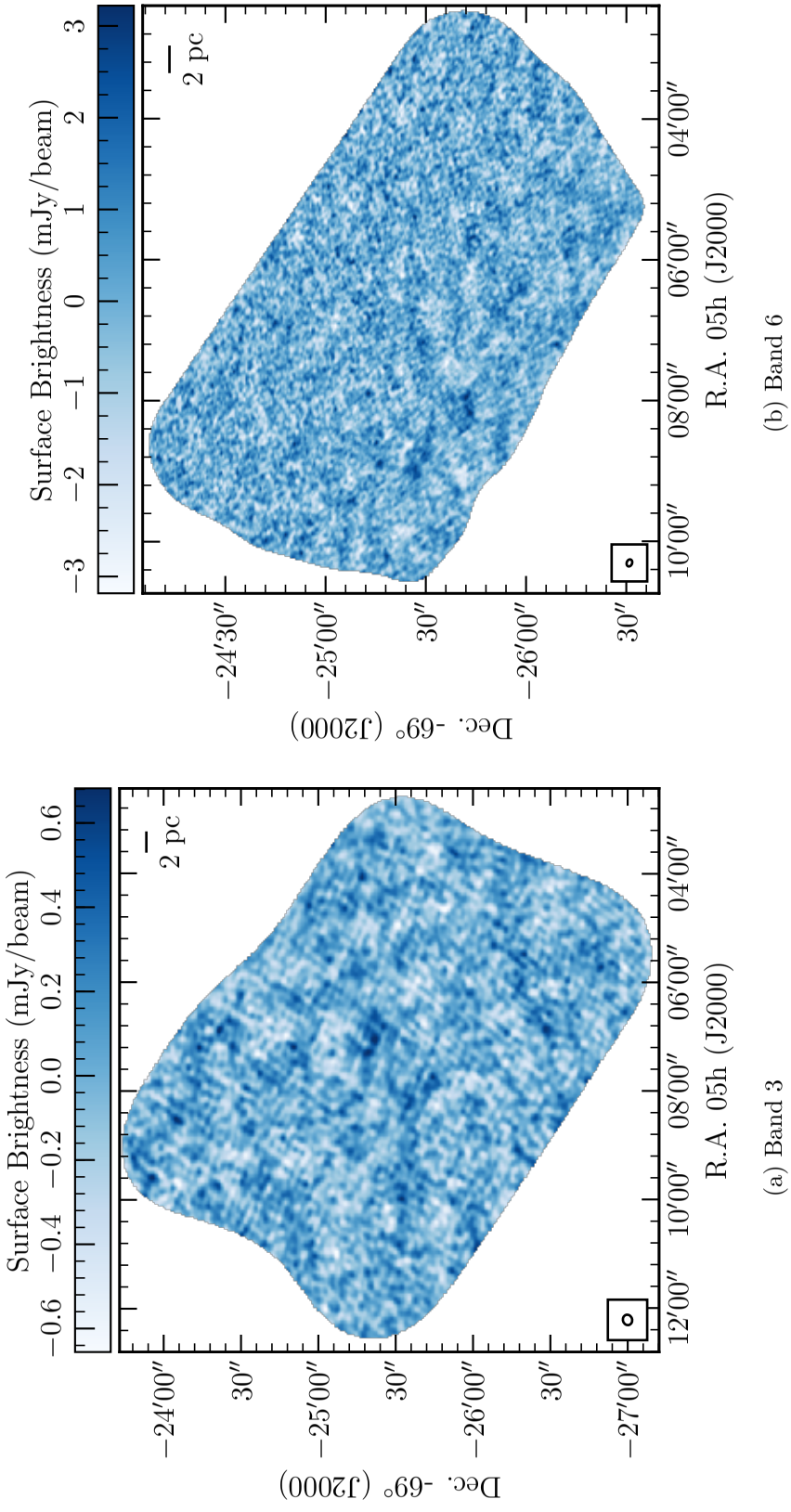

(a) Band 3

(b) Band 6

Figure 2.9: Dirty ALMA continuum maps of N166.

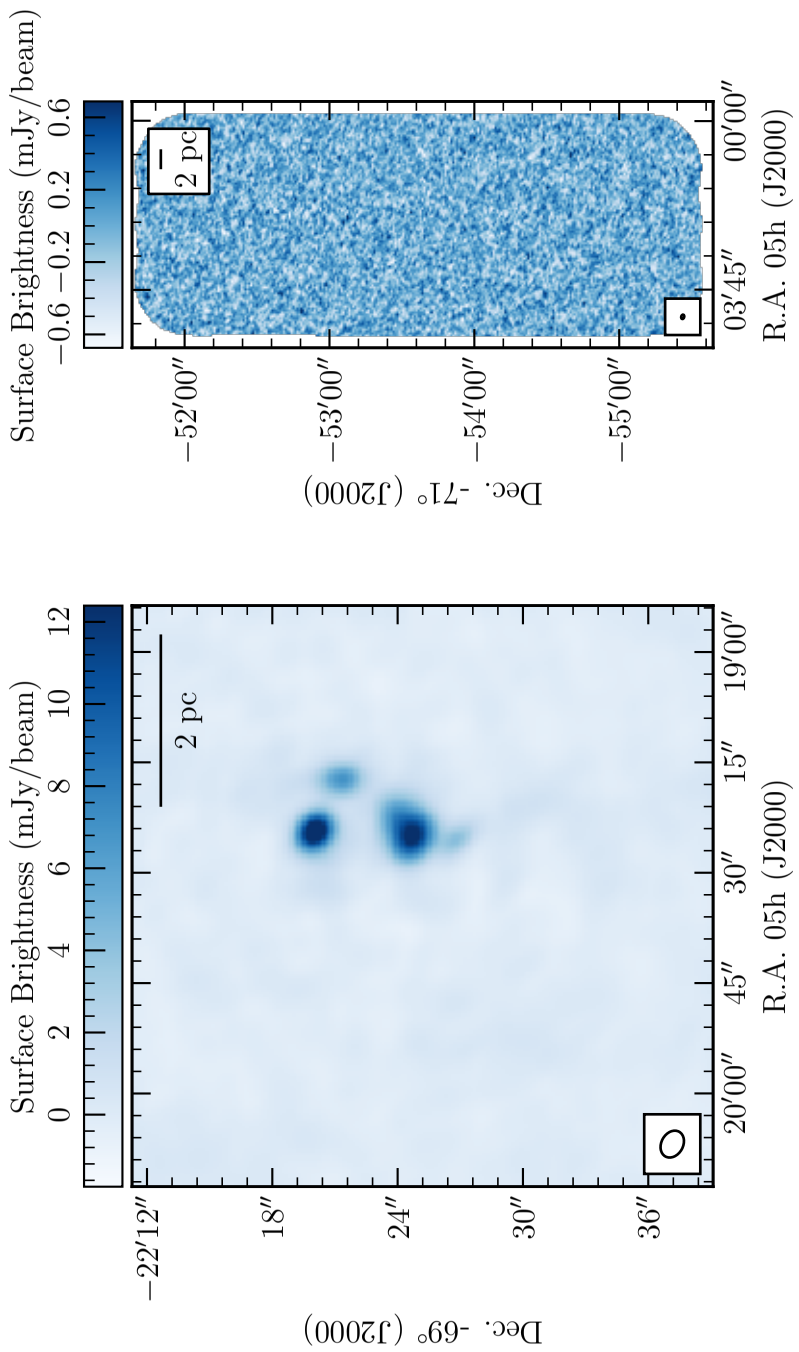

(a) N113

(b) PCC 11546

Figure 2.10: *(a)* Cleaned Band 6 ALMA map continuum of N113. *(b)* Dirty Band 6 ALMA continuum map of PCC 11546.

Chapter 3

Data Analysis

3.1 Free-Free Correction

Given the frequencies of these observations we expect the main contributions to continuum emission to be blackbody dust emission and free-free (Bremsstrahlung) emission. Dust emission originates from the cold ∼30 K dust throughout the molecular clouds emitting broadband thermal light peaking in the far infrared. Free-free emission is present due to the gas within the ISM being ionized by UV radiation from massive stars already present in and around the molecular clouds. Those freed electrons then interact with free protons producing light with a wide range of frequencies.

It is likely that the Band 3 continuum measurements are dominated by free-free emission, and in Band 6 the continuum is mostly thermal dust with a smaller contribution from free-free. Figure 3.1 illustrates this arrangement with a hypothetical spectral energy distribution (SED) containing free-free and dust components for ALMA's Bands 3 and 6. The dust emission can be used to estimate the total mass of the clumps in these fields but contamination from

free-free emission needs to be accounted for first.

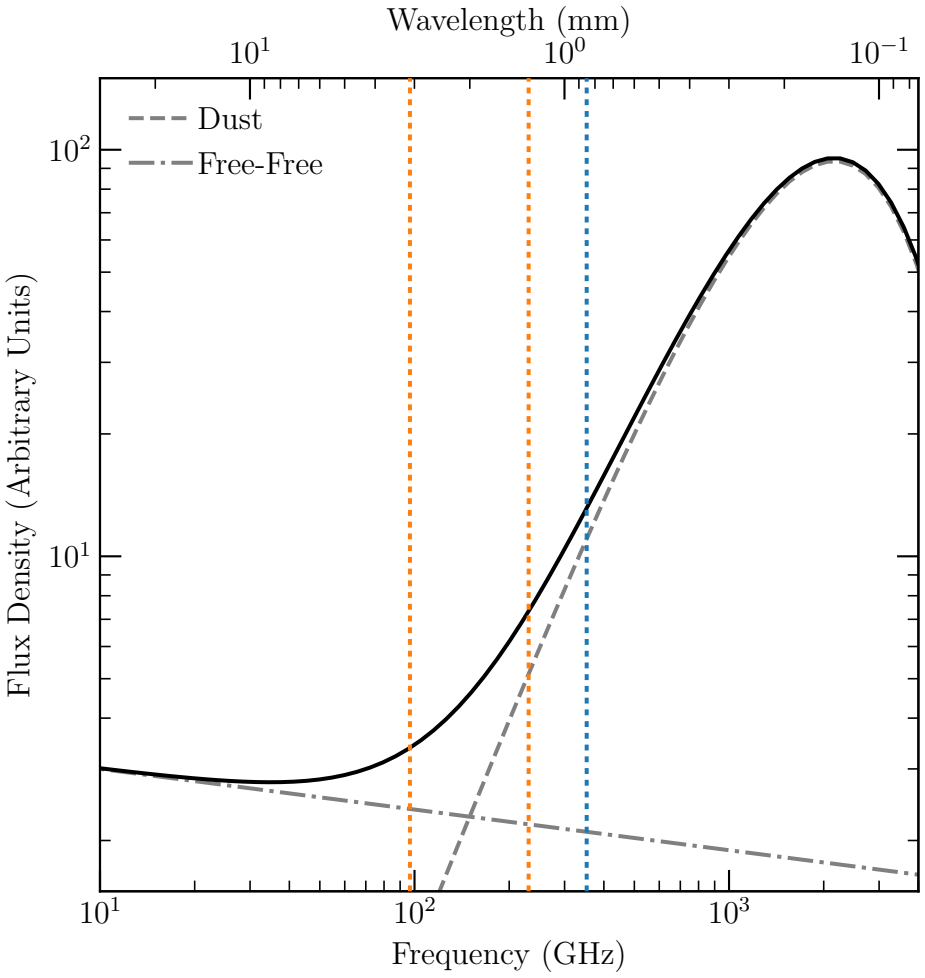

Figure 3.1: Hypothetical star forming region SED showing contributions from thermal dust and free-free emission. Vertical lines mark the ALMA observing Bands 3, 6, and 7 going from left to right.

To test the necessity of removing a free-free contribution to the Band 6 maps we compared flux densities of clumps in both bands. The clumps were identified in the Band 6 maps and flux densities were integrated over those regions in both bands (see Section 3.2 for details on clump identification). We used the same parameter settings as our dust-only clump finding except using the Band 6 dirty map RMS here. Figure 3.2 shows the results in 30

Dor-10, N159W and N159E. A dashed line shows the flux scaling for free-free emission with exponent -0.1 and two lines show dust emission with exponents $(2+\beta)$ for $\beta = 1$ and $\beta = 2$. The two dust lines should bracket the range of commonly quoted realistic emissivity indices (Gordon et al. 2014). Since the points are clustered between the free-free and dust scaling relations we conclude that the emission cannot be solely from thermally emitting dust. With an algebraic combination of the two frequency measurements we corrected for the contribution from free-free emission and constructed dust-only emission maps.

If we assume that the dominant contributions to emission are only dust and free-free, then for the Band 6 measurement we can write

$$S_{\rm B6} = S_{\rm d} + S_{\rm ff} \tag{3.1}$$

where $S_{\rm B6}$ is the Band 6 flux density, $S_{\rm d}$ is the dust-only flux density, and $S_{\rm ff}$ is the free-free-only flux density. For the Band 3 emission we can assume the same contributions but to scale the dust and free-free emission from the Band 6 emission we write

$$S_{\rm B3} = S_{\rm d}\left(\frac{\nu_{\rm B3}}{\nu_{\rm B6}}\right)^{(2+\beta)} + S_{\rm ff}\left(\frac{\nu_{\rm B3}}{\nu_{\rm B6}}\right)^{-0.1} \tag{3.2}$$

where $S_{\rm B3}$ is the Band 3 flux density, $\nu_{\rm B3}$ is the central frequency in Band 3, $\nu_{\rm B6}$ is the central frequency in Band 6, and β is the emissivity spectral index of the dust. The expression for the dust-only emission from solving Equations 3.1 and 3.2 is then

$$S_{\rm d} = S_{\rm B6} - \frac{S_{\rm B3} - S_{\rm B6}\left(\frac{\nu_{\rm B3}}{\nu_{\rm B6}}\right)^{(2+\beta)}}{\left(\frac{\nu_{\rm B3}}{\nu_{\rm B6}}\right)^{-0.1} - \left(\frac{\nu_{\rm B3}}{\nu_{\rm B6}}\right)^{(2+\beta)}}. \tag{3.3}$$

With this we produced dust-only emission maps for our fields so we could

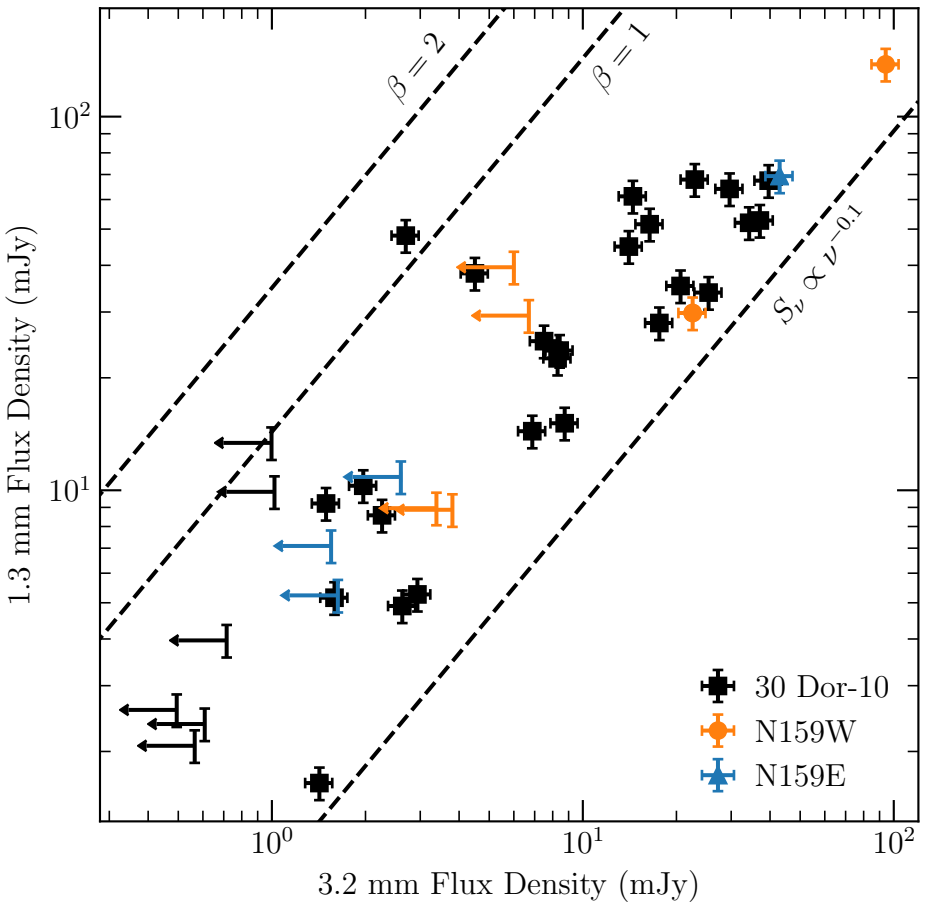

Figure 3.2: Comparison of Band 3 to Band 6 flux densities for clumps identified in Band 6. Dashed lines show free-free and two different thermal dust emission scaling relations. The two dust lines should bound the range of realistic dust emissivity spectral indices. Upper limits in Band 3 are for clumps found in Band 6 without significant co-spatial emission in Band 3. 10 % error bars are shown.

calculate accurate dust masses. We calculated an average value for the dust emissivity spectral index of $\beta = 1.49$ used on all of our maps from the Gordon et al. (2014) LMC-wide dust SED fits to Herschel observations. How we calculated this value is described further in Appendix C. Dust-only maps for 30 Dor-10, N159W, and N159E are shown in Figures 3.3 and 3.4.

Another possible source of continuum emission at these frequencies is synchrotron radiation from relativistic electrons spiraling along magnetic field lines. Without additional measurements to constrain its contribution our dust-only maps will still contain some synchrotron emission and therefore our dust emission (and masses) will be overestimated. This effect is likely to be small, however, as HII regions, forming stars, and young stars do not produce much synchrotron emission (Ginsburg et al. 2016). Given the physical size of our synthesized beams, the beam filling factor from this emission should be quite low.

Independently forming stars may not produce much synchrotron emission but colliding-wind binaries have been observed with spectral indices indicative of synchrotron radiation from particles accelerating in the wind collision zone (De Becker & Raucq 2013). To get a rough handle on the impact of such objects in our Band 3 observations we follow the estimate of Ginsburg et al. (2016). They quote colliding-wind binary radio luminosities in the range 10^{29} to 10^{30} erg s^{-1} from De Becker & Raucq (2013) resulting in flux densities at the distance to the Galactic star forming region W51 of 0.5 mJy to 5 mJy at 5 GHz. If we scale this upper value to the distance to the LMC (about 10 times more distant), the estimated flux density is 50 µJy. Then scaling this flux from 5 GHz to the frequency of our observations at 95 GHz gives ∼6 µJy. Comparing this to the uncertainties on our clump integrated flux densities in

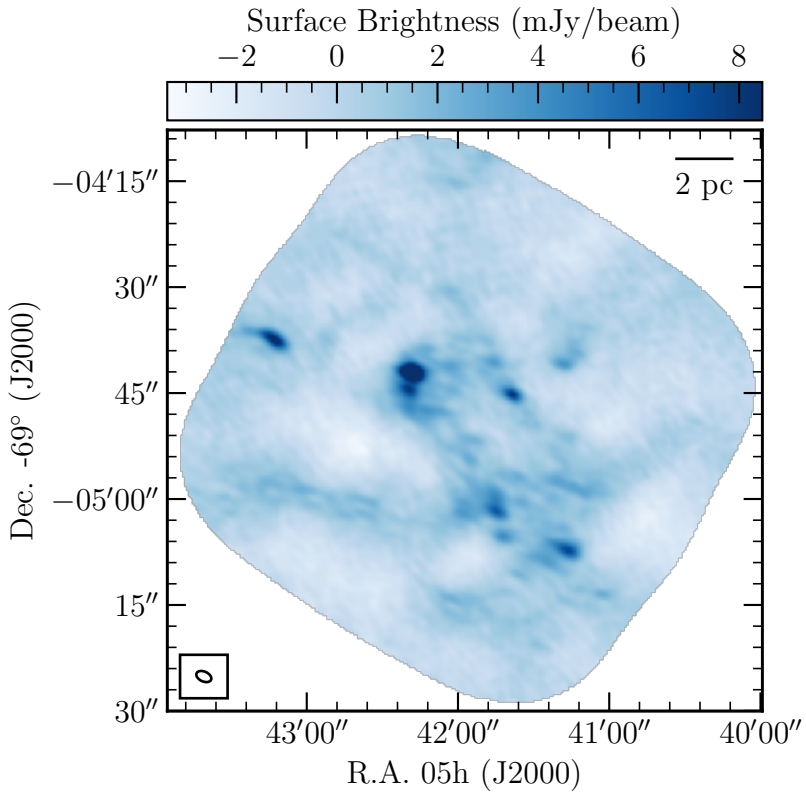

Figure 3.3: Dust-only map of 30 Dor-10.

Table 3.2 shows it is two orders of magnitude smaller than the smallest flux densities we detect as clumps. This means it would take about 100 of these binaries to affect our measurements and since these are massive stars it seems unlikely we would be observing such large groups of them. However, we still discuss ways to account for this synchrotron emission contamination in future work in Section 4.4.

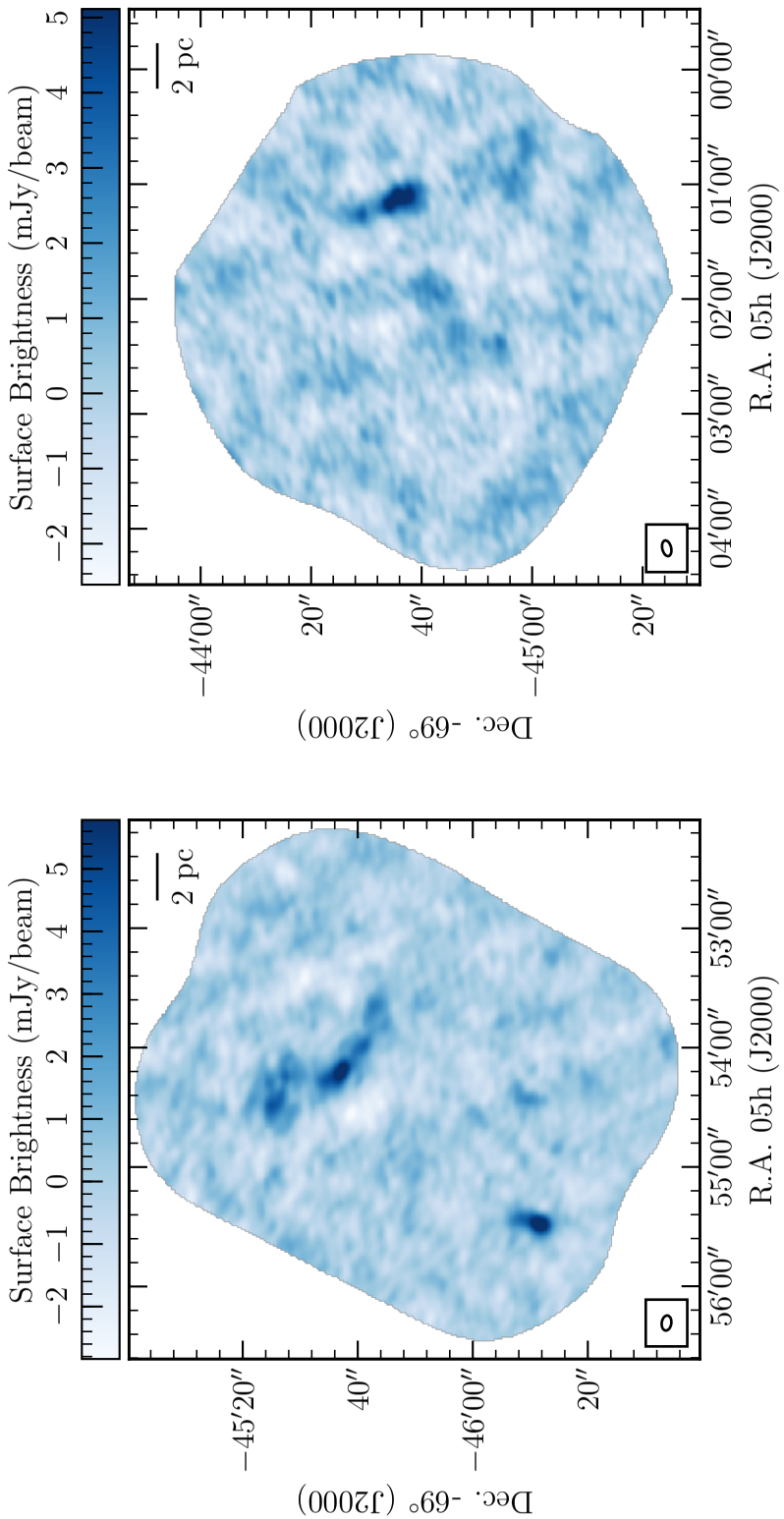

(a) N159W

(b) N159E

Figure 3.4: Dust-only maps of *(a)* N159W and *(b)* N159E.

3.2 Clump Finding

To identify molecular gas clumps in our dust-only maps we used the ClumpFind algorithm available in Starlink[1] through the Cupid package (Berry et al. 2007) and originally described by Williams et al. (1994). We chose to use this clump finding algorithm to make direct comparisons with previous works which also used ClumpFind. The settings we input to the algorithm were the dust-only map RMS, the beam FWHM, the minimum number of pixels required to accept an isolated clump, the lowest contour, the spacing between contours, the flag to not do background subtraction, the flag to not deconvolve the clumps and the flag to return clump parameters such as on-sky sizes and locations using the world coordinate system (WCS) information. A total of 32 dust clumps were identified in the three fields 30 Dor-10, N159W and N159E with the majority found in 30 Dor-10 (see Table 3.2 for a field-by-field summary of the clump finding results).

Briefly, ClumpFind works by contouring the map based on the selected inputs and then starts with the highest contour, searching for peaks. Clusters of pixels around a peak are assigned to a clump through a friends-of-friends approach. Then the next lowest contour is searched for significant pixels which are then either collected into a new clump or assigned to a previously identified clump based on proximity. New clumps are added at all contour levels except the lowest. Pixels are added to clumps at all contour levels. The number of pixels in each clump is then compared to the number that would be in a circular Gaussian clump with FWHM the same as the input FWHM and reduced to account for only considering the area with pixel values above the

[1]The Starlink software (Currie et al. 2014) is currently supported by the East Asian Observatory.

lowest input contour. Those with too few pixels are discarded. Lastly, a check of the returned size of each clump against the input FWHM is done to again attempt to reject clumps that are too small compared to the resolution of the observations.

The RMS we input to ClumpFind was measured in each dust-only map in a region where no obvious emission, artifacts or negative bowls were visible. The lowest contour was always set to three times the map RMS to ensure pixels could be trusted with some confidence while also trying to recover most of the emission associated with a clump. Contour spacings were always set to two times the RMS as this minimized needlessly splitting up sources while still recovering most of the obvious features. This combination of lowest contour level and contour spacing was also shown to result in the lowest number of missed and "false" clumps through synthetic source detection testing by Williams et al. (1994). Our own testing with several choices for these two settings showed that our final choice gave results that picked out distinct but somewhat blended sources without extracting spurious looking sources, along with staying well within believable bounds around obvious sources. Background subtraction was not used due to the interferometer's intrinsic spatial filtering removing large-scale emission as well as the complicated interplay of bright emission causing adjacent negative regions. Clump parameters were reported using the WCS information from the maps for convenience.

During testing of our completeness estimation code (described in Section 3.3.3) we found that our setting for the beam FWHM parameter to ClumpFind caused the algorithm to reject sources as too small when it should not have done so. We were setting the beam FWHM as the geometric mean of the major and minor axes of our elliptical synthesized beams and the syn-

Table 3.1: Summary of clump finding.

Field	N Clumps	Max. Mass ($M_\odot$)	Min. Mass ($M_\odot$)	RMS ($M_\odot$)	Complete[a] ($M_\odot$)	`minpix`
30 Dor-10	22	5740 ± 220	205 ± 48	45	210	56
N159W	7	3200 ± 260	530 ± 140	85	260	”
N159E	3	2320 ± 180	570 ± 110	72	320	61

[a] 50 % completeness mass reported.

thetic sources we were using for completeness testing were circular Gaussians with FWHM set to that same geometric mean. To avoid this problem we instead set the FWHM parameter to zero and specified the `minpix` parameter for rejecting clumps that were too small. This turned out to give the same resulting clumps as when using the FWHM parameter but it prevented clumps near the size of the beam from being rejected as too small due to the lowest contour setting (Private Email Communication from Dr. David Berry of Joint Astronomy Centre and East Asian Observatory). To determine what to input for `minpix` we would simply run ClumpFind once with FWHM set to the geometric mean of the synthesized beam axes, note the minpix value ClumpFind would calculate internally, discard those clump finding results, and run ClumpFind a second time with FWHM set to zero and `minpix` set to the number of pixels reported in the first run. As this could allow clumps that were of the same area as the synthesized beam but smaller dimensions along R.A. and Dec. (e.g. long and skinny clumps) we made sure to inspect the clump regions identified with ClumpFind visually for each field. Clump sizes were not deconvolved because of this setting of the FWHM. Values for `minpix` are summarized per field in Table 3.1.

Table 3.2: Clump property summary.

Name	R.A.[a] (J2000)	Dec.[a] (J2000)	Area[b] (pc^2)	S_{peak}[c] (mJy/beam)	S_{int}[d] (mJy)	M ($M_\odot$)
30 Dor-10 1	05:38:49.22	-69:04:42.24	2.6	19.7	53.9 ± 1.5	5660 ± 160
30 Dor-10 2	05:38:52.84	-69:04:37.55	1.8	9.5	26.6 ± 1.3	2750 ± 140
30 Dor-10 3	05:38:46.56	-69:04:45.30	1.5	8.3	18.3 ± 1.2	1890 ± 120
30 Dor-10 4	05:38:49.32	-69:04:44.40	3.4	8.3	45.0 ± 1.8	4650 ± 180
30 Dor-10 5	05:38:45.08	-69:05:07.26	3.7	7.5	43.8 ± 1.9	4530 ± 190
30 Dor-10 6	05:38:47.00	-69:05:01.68	4.9	6.7	55.6 ± 2.1	5740 ± 220
30 Dor-10 7	05:38:46.83	-69:05:05.28	0.97	4.2	9.80 ± 0.93	1012 ± 96
30 Dor-10 8	05:38:45.22	-69:04:40.98	1.2	3.8	10.8 ± 1.1	1110 ± 110
30 Dor-10 9	05:38:47.06	-69:04:40.80	1.4	3.4	11.9 ± 1.2	1230 ± 120
30 Dor-10 10	05:38:48.21	-69.04.41.16	1.5	3.1	12.8 ± 1.2	1330 ± 120
30 Dor-10 11	05:38:44.98	-69.04.58.26	3.1	3.1	26.7 ± 1.7	2760 ± 170
30 Dor-10 12	05:38:47.70	-69.04.54.30	0.75	2.7	6.33 ± 0.82	650 ± 85
30 Dor-10 13	05:38:46.39	-69.04.57.00	0.78	2.6	6.83 ± 0.84	705 ± 87
30 Dor-10 14	05:38:44.21	-69.05.13.38	0.53	2.6	4.10 ± 0.69	424 ± 72

Continued on next page

[a] Positions are peak positions as reported by ClumpFind.

[b] Calculated from the "square arcseconds" value reported by ClumpFind.

[c] Uncertainties are random statistical uncertainties measured from each dust map and are the same for all clumps in a field: 0.4 mJy/beam for 30 Dor-10, 0.8 mJy/beam for N159W and 0.7 mJy/beam for N159E.

[d] Uncertainties are calculated by combining uncertainties in each band through the partial differential propagation of Equation 3.3. Uncertainties in each band are the RMS noise in each band times the square root of the number of beams covering the clump area in the dust-only map.

Table 3.2: *continued*

Name	R.A.[a] (J2000)	Dec.[a] (J2000)	Area[b] (pc^2)	S_{peak}[c] (mJy/beam)	S_{int}[d] (mJy)	M ($M_\odot$)
30 Dor-10 15	05:38:52.14	-69.04.58.62	1.4	2.5	10.4 $\pm$ 1.1	1070 $\pm$ 120
30 Dor-10 16	05:38:48.14	-69.05.14.10	1.5	2.3	11.1 $\pm$ 1.2	1150 $\pm$ 120
30 Dor-10 17	05:38:47.60	-69.04.51.78	0.53	2.3	4.32 $\pm$ 0.69	447 $\pm$ 71
30 Dor-10 18	05:38:50.29	-69.05.00.42	1.4	2.2	10.3 $\pm$ 1.1	1060 $\pm$ 120
30 Dor-10 19	05:38:45.52	-69.04.59.70	0.64	2.2	5.07 $\pm$ 0.76	524 $\pm$ 78
30 Dor-10 20	05:38:53.05	-69.04.57.53	1.6	2.2	11.8 $\pm$ 1.2	1220 $\pm$ 130
30 Dor-10 21	05:38:46.36	-69.05.10.68	0.31	2.1	2.41 $\pm$ 0.53	249 $\pm$ 55
30 Dor-10 22	05:38:45.96	-69.04.58.44	0.24	2.1	1.98 $\pm$ 0.47	205 $\pm$ 48
N159W 1	05:39:41.90	-69.46.11.48	2.0	8.4	25.2 $\pm$ 2.2	2610 $\pm$ 230
N159W 2	05:39:36.77	-69.45.37.41	2.7	7.6	31.0 $\pm$ 2.6	3200 $\pm$ 260
N159W 3	05:39:37.96	-69.45.25.27	3.3	4.6	28.0 $\pm$ 2.8	2890 $\pm$ 290
N159W 4	05:39:35.95	-69.45.41.03	1.4	4.2	12.3 $\pm$ 1.9	1270 $\pm$ 190
N159W 5	05:39:36.93	-69.45.27.40	1.5	4.0	12.5 $\pm$ 1.9	1290 $\pm$ 200
N159W 6	05:39:34.63	-69.45.42.94	1.5	3.3	11.1 $\pm$ 1.9	1150 $\pm$ 190
N159W 7	05:39:37.75	-69.46.09.57	0.73	2.8	5.1 $\pm$ 1.3	530 $\pm$ 140
N159E 1	05:40:04.47	-69.44.35.88	1.8	6.6	22.4 $\pm$ 1.7	2320 $\pm$ 180
N159E 2	05:40:04.71	-69.44.34.41	0.75	6.0	8.7 $\pm$ 1.1	900 $\pm$ 120
N159E 3	05:40:05.08	-69.44.29.37	0.65	3.9	5.5 $\pm$ 1.0	570 $\pm$ 110

3.3 LMC Clump Mass Function

An empirical mass distribution is typically plotted as either a differential mass function or a cumulative mass function. The differential mass function is shown in Equation 1.3 and is calculated by simply defining mass bins spanning the mass range of objects and counting the number within each bin. This form affords a simple Poissonian counting statistics approach to uncertainties for fitting but the choice of bin widths and centers is unconstrained so the results may depend on the bin choices. The cumulative mass function, shown in Equation 1.1, avoids complications from binning choices as it is just an ordered tally of masses at or above a given object's mass. The trade off is that there is not a simple statistical approach to handling uncertainties for fitting, but there are ways to overcome this as we discuss in Section 3.3.3. Note that the power law index α of Equation 1.3 is the same power law index as from Equation 1.1 (i.e. Salpeter 1955, $\alpha = -2.35$ for both differential and cumulative mass functions).

Since we were working with a small sample of clumps we chose to calculate and fit the cumulative form so that we can avoid very small numbers of clumps in each mass bin. Our process for calculating the cumulative clump mass function for 30 Dor-10, N159W and N159E is given here along with fitting, uncertainty, and completeness considerations.

3.3.1 Converting Dust Flux To Total Gas Mass

We calculate total mass (gas plus dust) for each of the dust clumps identified in our dust-only maps. Clump flux densities were converted to dust masses

using

$$M_{\rm d} = \frac{Sd^2}{\kappa B(T_{\rm d})} \tag{3.4}$$

where S is the dust flux density integrated over the spatial extent of the clump, d is the distance to the LMC, κ is the dust opacity per unit mass column density, and $B(T_{\rm d})$ is the Planck function evaluated at the dust temperature $T_{\rm d}$. Given the distance measurement from Pietrzyński et al. (2013) of (49.97 ± 1.11) kpc we simply adopted a distance of 50 kpc for our calculations. The dust temperature and opacity were calculated from the Gordon et al. (2014) temperature and emissivity maps where we averaged the pixel values covering 30 Dor-10, N159W, N159E and N113 for a temperature of 36.7 K and an opacity of $1.16\,{\rm cm^2\,g^{-1}}$. More details are given in Appendix C.

With the dust mass calculated using Equation 3.4 we applied a conversion to total gas mass through a gas-to-dust (G/D) ratio of 500 from Roman-Duval et al. (2017). This G/D ratio is obtained by stacking the dust SEDs across the entire LMC as measured with IRAS and Planck in bins of varying gas surface density. This is after foreground Milky Way cirrus emission has been subtracted. Atomic gas surface densities are derived from 21 cm Parkes observations (Staveley-Smith et al. 2003) and molecular gas is derived from ^{12}CO (1-0) NANTEN observations (Mizuno et al. 2001). The stacked SEDs are fitted with a modified blackbody to estimate the dust surface density, as well as the temperature and spectral emissivity index. Then the ratio of the dust surface density to the gas surface density is the G/D ratio, in each interval of gas surface density. We chose their G/D in the highest surface density bins as this is likely where stars are forming.

Figure 3.5 shows the LMC mass function as calculated from the Band 6 map

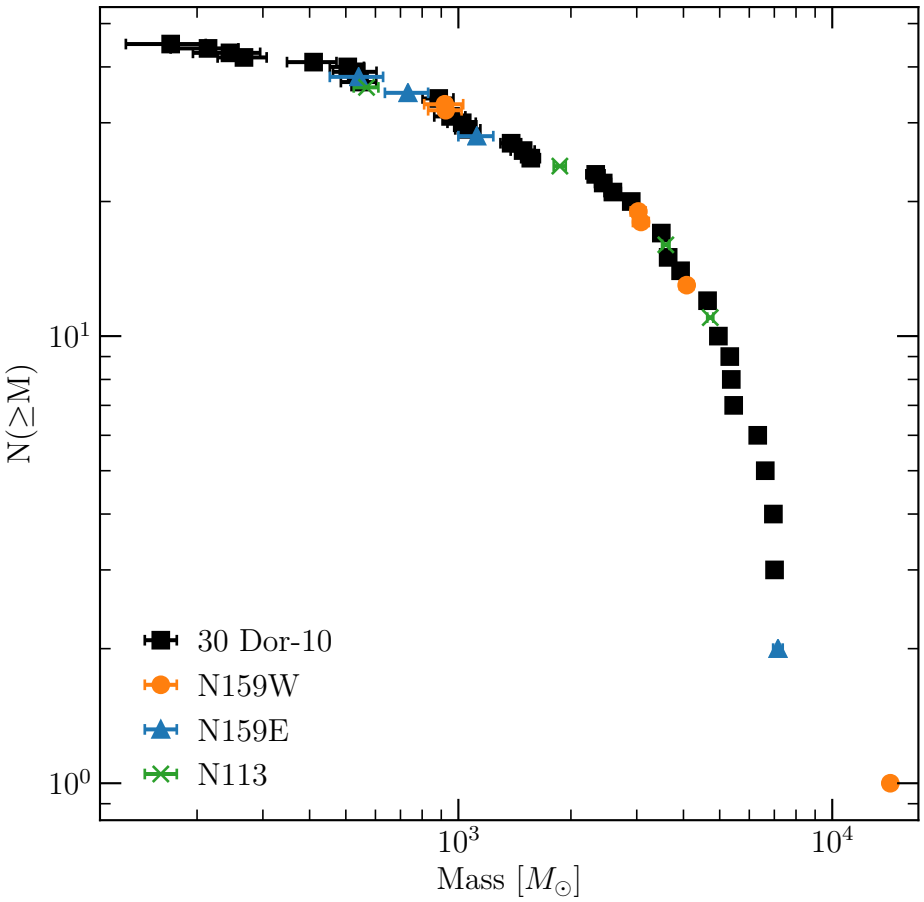

Figure 3.5: Clump mass function from Band 6 maps of 30 Dor-10, N159W, N159E and N113. Masses are calculated assuming Band 6 flux arises solely from thermal dust emission.

directly, not accounting for the free-free contamination. Figure 3.6 adds the dust-only clump mass function with the Band 6 mass function for comparison.

3.3.2 Functional Fitting

A common model for the cumulative mass function of clumps and cores is a broken power law with parameters for two independent power law indices and a break mass where the power laws transition from one to the other. This can

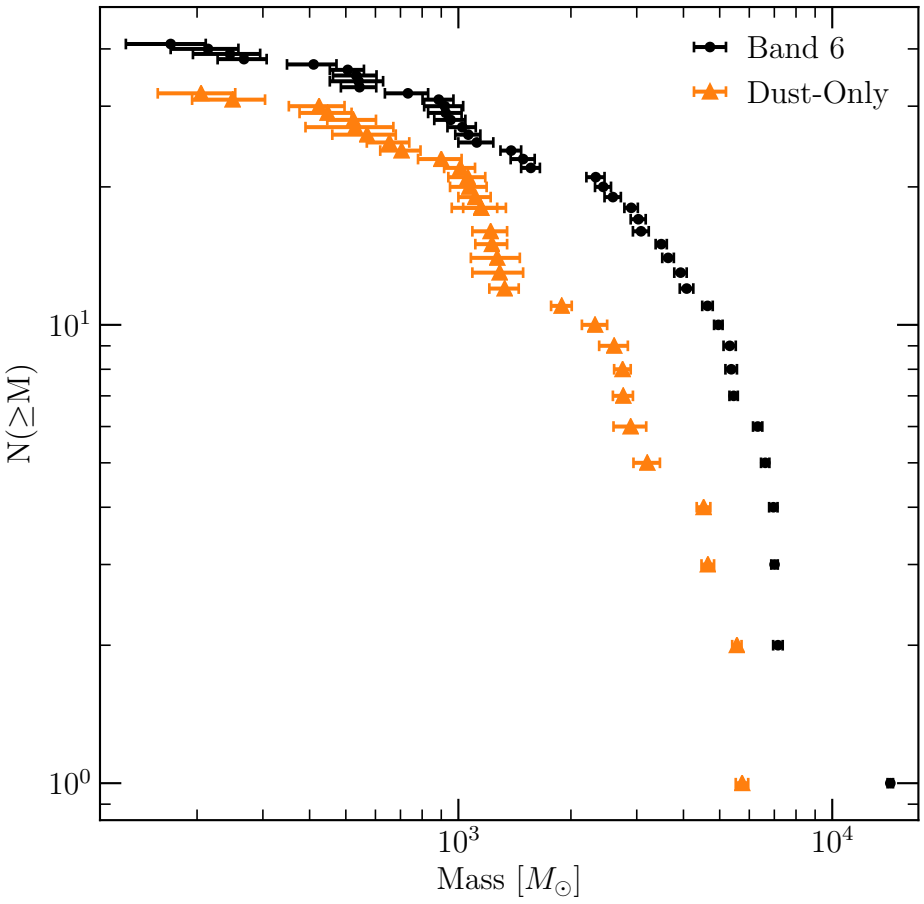

Figure 3.6: Comparison of clump mass functions from Band 6 maps and dust-only maps. N113 clumps are excluded from the Band 6 mass function in this plot.

Table 3.3: Clump mass function fitting results.

	$\alpha_{\rm low}$	$\alpha_{\rm high}$	$M_{\rm break}$
Initial Guess	-1.8	-3.5	2500
Raw Mass Function	$-1.5^{+0.2}_{-0.1}$	$-3.3^{+0.3}_{-0.4}$	2200^{+400}_{-300}
$> 500\,{\rm M}_\odot$	$-1.74^{+0.05}_{-0.2}$	$-3.3^{+0.3}_{-0.8}$	2500^{+900}_{-300}
Completeness Corrected	$-1.76^{+0.07}_{-0.1}$	$-3.3^{+0.3}_{-0.6}$	2500^{+700}_{-300}

be written as

$$N(\geq M) = \begin{cases} AM_{\rm break}^{(\alpha_{\rm high}-\alpha_{\rm low})} M^{(\alpha_{\rm low}+1)} & M < M_{\rm break} \\ AM^{(\alpha_{\rm high}+1)} & M \geq M_{\rm break} \end{cases} \tag{3.5}$$

where A is an arbitrary amplitude, $M_{\rm break}$ is the break mass where the power law index changes, $\alpha_{\rm low}$ is the power law index for masses below $M_{\rm break}$, and $\alpha_{\rm high}$ is the power law index for masses above $M_{\rm break}$ (Reid & Wilson 2006a).

Given our relatively small sample of clumps and the simple (read few parameters) model, we chose to carry out our fitting with the standard nonlinear Levenberg-Marquardt least-squares minimization (More 1977). This is done with the SciPy v0.19.0 (Jones et al. 2001–) `optimize.curve_fit` function. Inputs were the double power law Python function to optimize, the clump masses, $N(\geq M)$, an initial guess for the parameters (see Table 3.3), `absolute_sigma` set to True, and the maximum number of iterations set to 10 000. To estimate fitting weights we followed the approach used by Reid & Wilson (2006b). The approximate weights for fitting a cumulative mass function can be found by first noting that the random mass uncertainties scale as $\sigma_M \propto M$ and by approximating the mass function as $N(\geq M) \simeq AM^{-x}$. They then write down

the standard propagated uncertainty for N through partial differentiation resulting in $\sigma_N \propto N$. So for the `sigma` input to `curve_fit` which specifies the vector of y-data uncertainties we used the cumulative number $N(\geq M)$ for each clump. The best fit double power law parameters are given in Table 3.3 for the mass function determined directly from the clump masses along with two variations that attempt to account for clump completeness (see Section 3.3.3 for further details). The procedure and inputs for fitting are the same across all three variations.

3.3.3 Uncertainty And Completeness Estimation

Given the form of the fitting function, there are only uncertainties in the x-variable. This renders the covariance matrix output of the SciPy function useful only in a relative sense for characterizing the resultant best fit parameter uncertainties. To estimate the absolute uncertainties on the parameters we used Monte Carlo simulation, as done by Reid & Wilson (2006b). This involved generating 10^5 artificial mass functions and fitting each in the same way as the ALMA measured mass function. From the distributions of fit parameters we took the inner 95 % to be the 2σ uncertainties on each fit parameter. The mass functions were made by drawing normally distributed random deviates whose distributions were centered on each measured clump mass and standard deviations were the measurement uncertainties on the masses from the dust-only maps. Then each newly generated sample of 32 masses was sorted into descending order to prepare for fitting. Not only does this Monte Carlo approach simplify estimating the fit parameter uncertainties but it also nicely includes the effects of neighboring masses swapping places in the sorted

order due to their uncertainties.

Figure 3.7 shows the distributions of the best fit parameters for the synthetic mass functions made from the mass function calculated from the observed clump masses. The distributions are nearly symmetric and Gaussian, except for the amplitude which exhibits a long tail at large values. The amplitude histogram is trimmed above the 90th percentile for ease of plotting. Table 3.3 shows the uncertainties for each best fit parameter.

To account for the finite depth and resolution of these observations we attempted to estimate the completeness of our mass function. This was accomplished through Monte Carlo techniques by injecting synthetic sources of known fluxes and sizes into the dust-only maps one at a time, running ClumpFind on the altered map with the same parameters as for the original maps and counting when synthetic clumps were recovered and when they were not. We then took the ratio of the number recovered to the total number injected as the completeness fraction. Synthetic source positions were randomly placed across the maps following a uniform distribution. All sources were elliptical Gaussians with the FWHM and position angle identical to the synthesized beam for the corresponding map. By dividing the area of the map by the area of the synthesized beam we found 600 sources would result in covering about half of each map. As this seemed like ample coverage for testing the completeness over the entire image we chose to inject 600 synthetic sources per mass bin. Synthetic source masses were spaced evenly in log-space from roughly $21\,M_\odot$ to $1.2 \times 10^4\,M_\odot$. Figure 3.8 shows the completeness curves for 30 Dor-10, N159W and N159E.

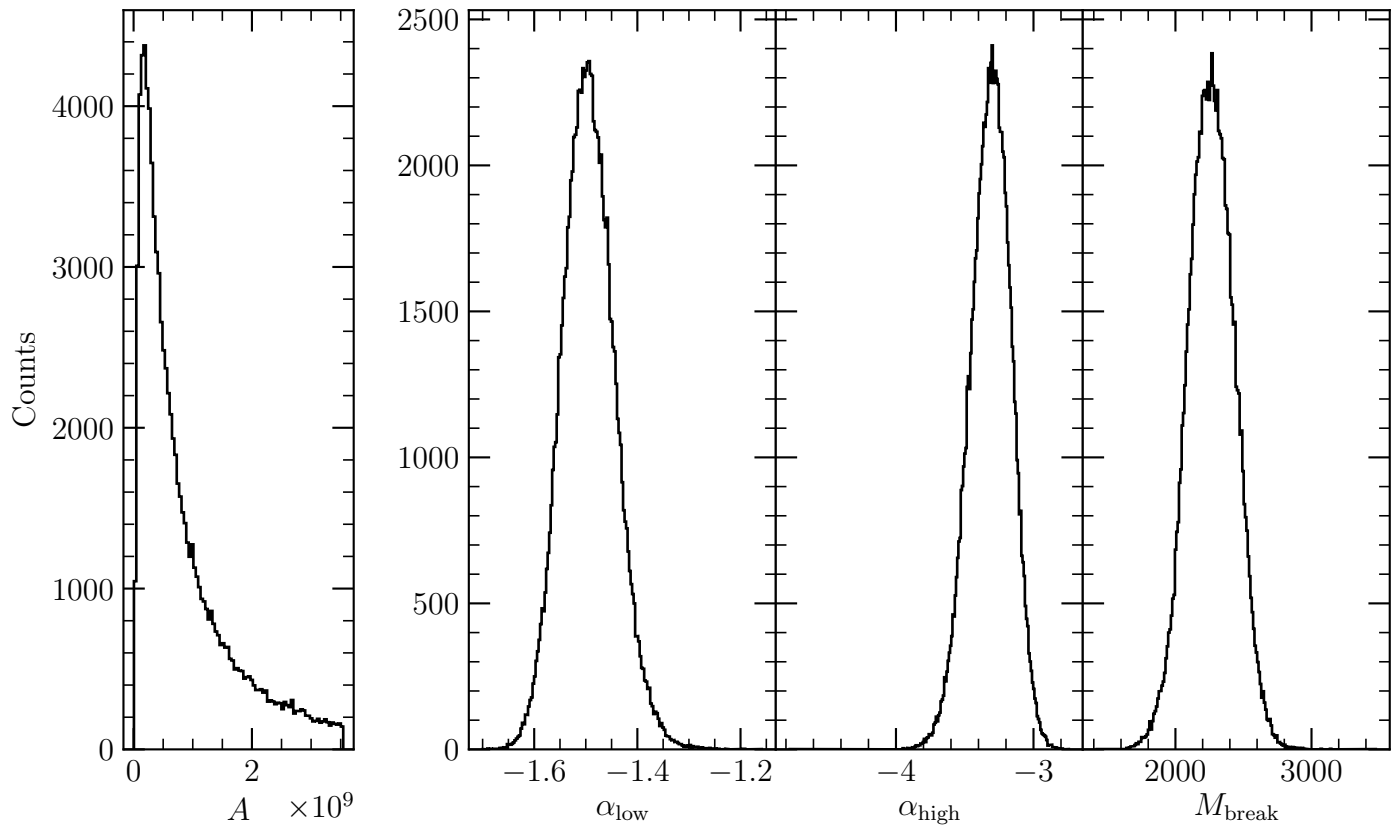

Figure 3.7: Distributions of best fit parameters from 10^5 artificial mass function realizations for the "raw" clump mass function. Amplitude histogram is trimmed above the 90th percentile for ease of plotting.

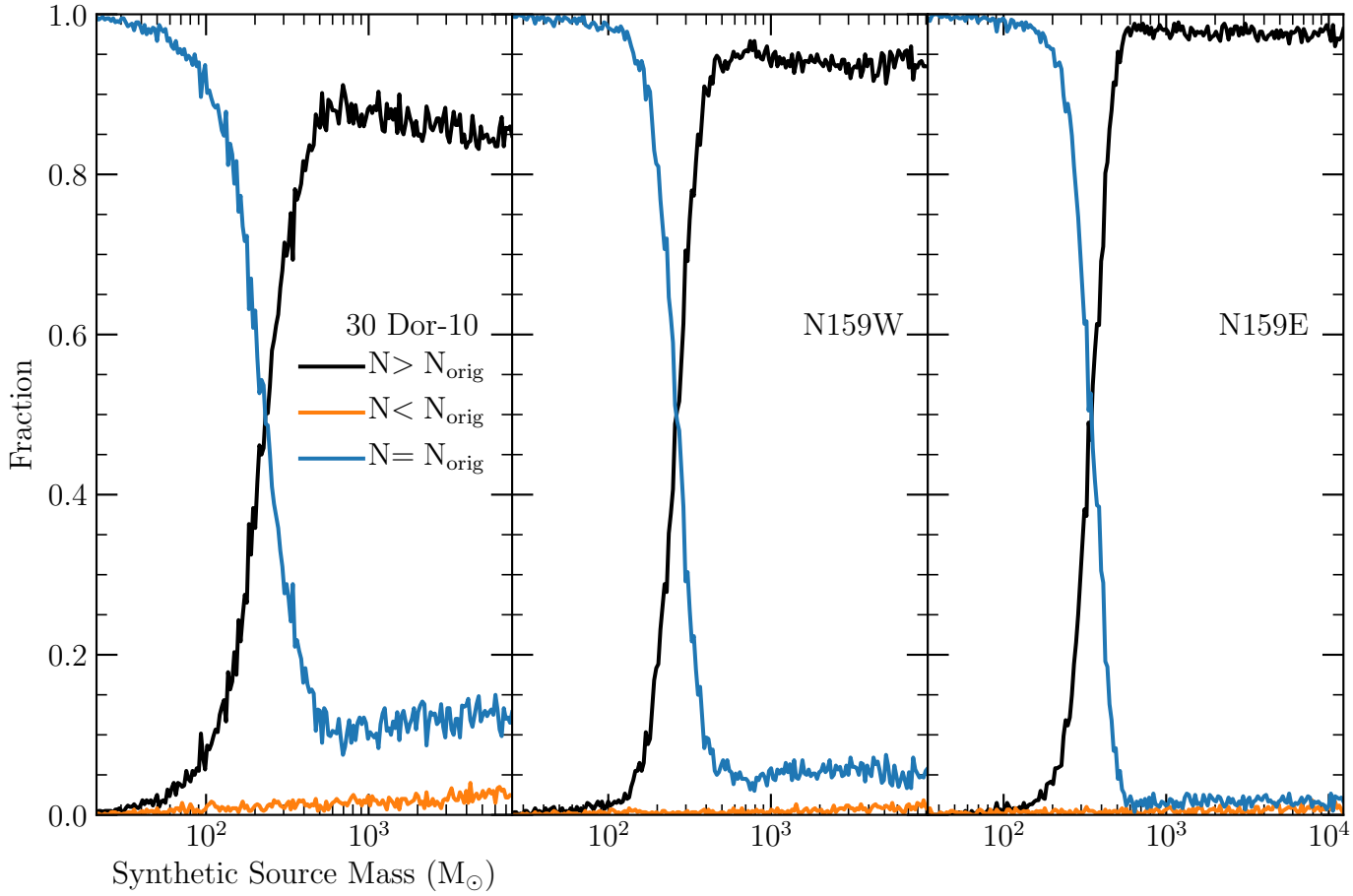

Figure 3.8: Fractions of synthetic source injections that resulted in the same number (blue), more (black), and less (orange) clumps found compared found to the original maps. Black is typically what is referred to as the completeness fraction.

Table 3.4: Logistic function best fit parameters for completeness curves.

Field	A	α	M_0
30 Dor-10	0.89	8.0	2.3
N159W	0.95	14	2.4
N159E	0.98	15	2.5

To estimate mass thresholds for a given completeness fraction we fit each completeness curve with a standard logistic function (Harris et al. 2016; Freeman et al. 2017)

$$f(M) = A\left\{1 + \exp\left[-\alpha\left(\log_{10}\frac{M}{\mathrm{M}_\odot} - M_0\right)\right]\right\}^{-1} \tag{3.6}$$

where $f(M)$ is the completeness fraction, A is an amplitude to allow fitting curves that do not asymptote to one, α controls the width of the central part of the curve and M_0 is the logarithm of the mass at which $f = 0.5A$. Figure 3.9 shows the best fits to each field's completeness and Table 3.4 gives the best fit parameters. With the best fit parameters, mass thresholds for a given completeness fraction were found by inverting equation 3.6. Table 3.1 reports the 50 % completeness masses for each field.

We chose to test two methods of accounting for the completeness of the maps. The first was to determine a mass threshold where we would only fit clumps with masses greater than the threshold. We decided on a threshold of $500\,\mathrm{M}_\odot$ since this is roughly where the 30 Dor-10 completeness curve flattens out at maximum completeness. We used the 30 Dor-10 completeness curve because it contributes the majority of the clumps in our mass function. Best fit parameters for this thresholded mass function are given in Table 3.3 and the distributions of synthetic mass function best fit parameters are shown in Figure 3.10.

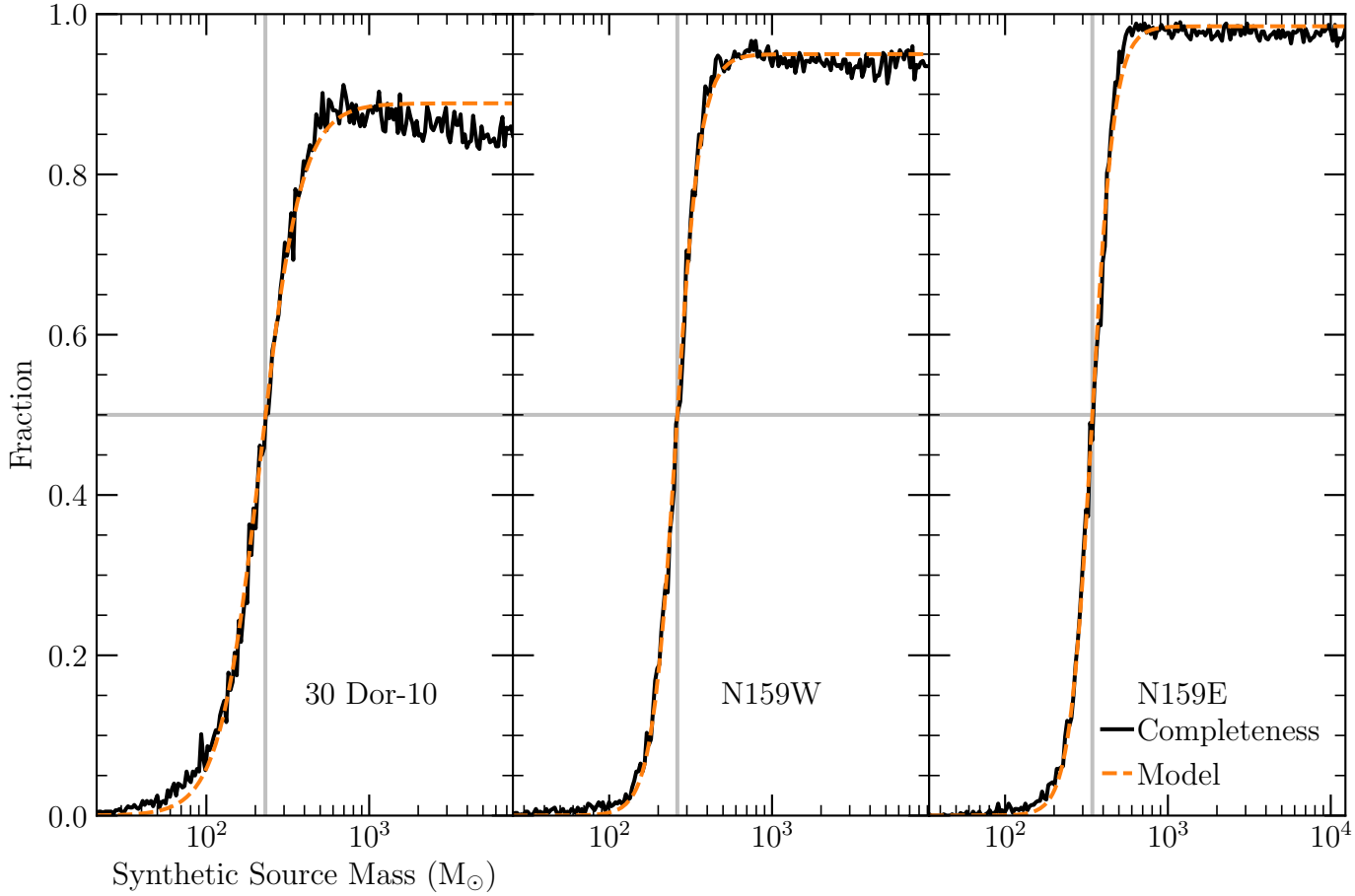

Figure 3.9: Logistic curve best fit for 30 Dor-10, N159W, and N159E. 50 % completeness marked by the gray lines.

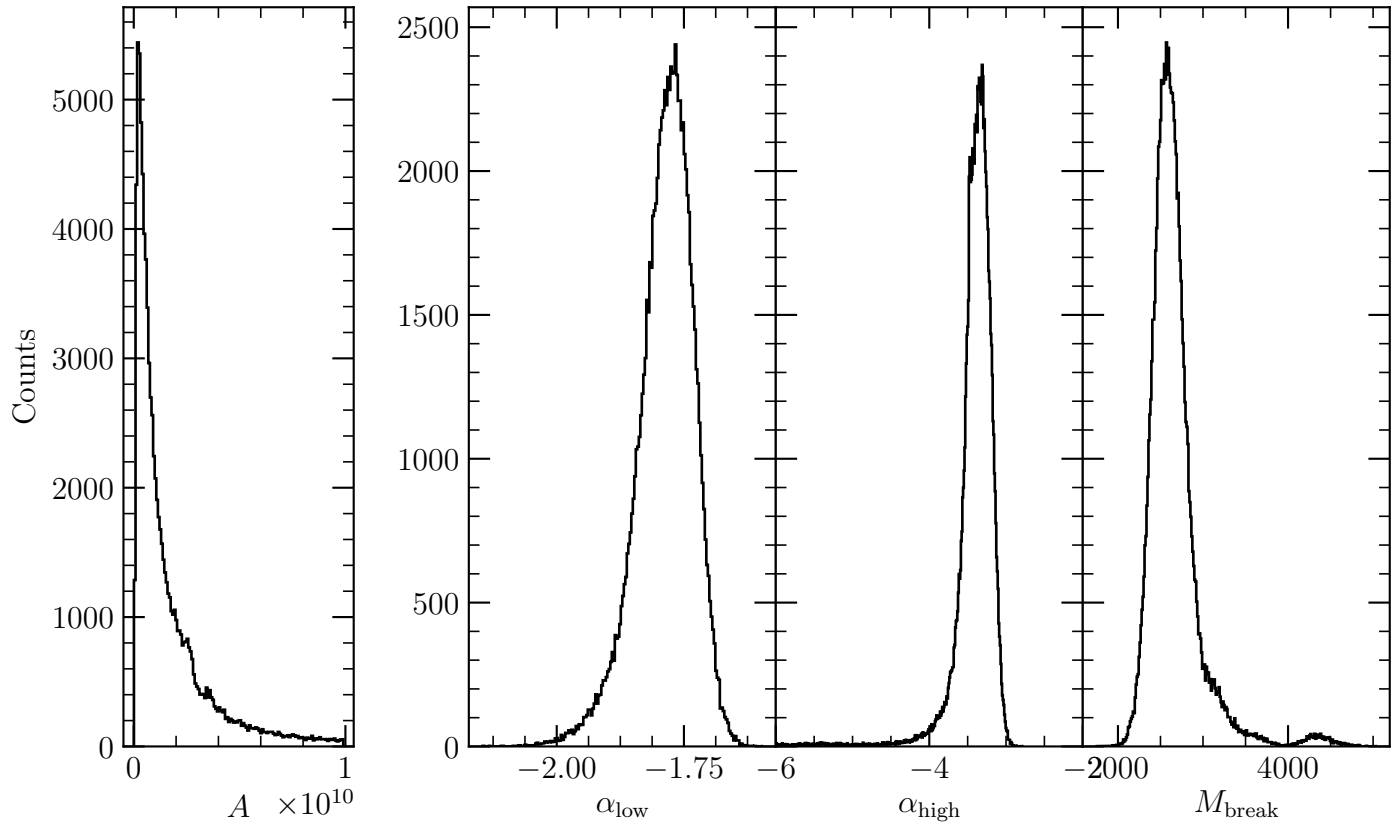

Figure 3.10: Distributions of best fit parameters from 10^5 artificial mass function realizations for clump mass function fit limited to masses above $500\,\mathrm{M}_\odot$. Amplitude histogram is trimmed above the 90th percentile for ease of plotting.

The second method was to use the logistic curve fit to the completeness curve to correct the mass function numbers and fit the corrected numbers. We again chose to use the 30 Dor-10 completeness curve. Applying this completeness correction resulted in the mass function shown as orange points in Figure 3.11 with a comparison to the mass function numbers directly calculated from the clump list in black points. Figure 3.12 shows the corrected mass function with each field marked separately along with the best fit double power law. We use all clumps in our sample in this fitting with our lowest mass of $205\,M_\odot$ at the 41 % complete level. The best fit parameters are in Table 3.3 and distributions of synthetic mass function best fit parameters are shown in Figure 3.13. It should be noted that the parameter distributions become somewhat less symmetric, primarily with a stronger tail on one side of the peak. The best fit double power laws for the two methods of accounting for completeness end up being statistically indistinguishable based on our Monte Carlo uncertainty estimation.

With a total mass (gas plus dust) clump mass function from the LMC derived from free-free emission corrected dust mass measurements we can compare to core and clump mass functions from star forming regions in the Milky Way. Using a double power law fit should afford us some extra flexibility when comparing to previous studies. Many Milky Way mass function fits include a power law component but typically for mass ranges much lower than our LMC clumps. If the clump masses we have measured are truly bridging the gap between cores and GMCs then it may be useful to have two power law indices fit to our curving mass function as we show in the following discussion.

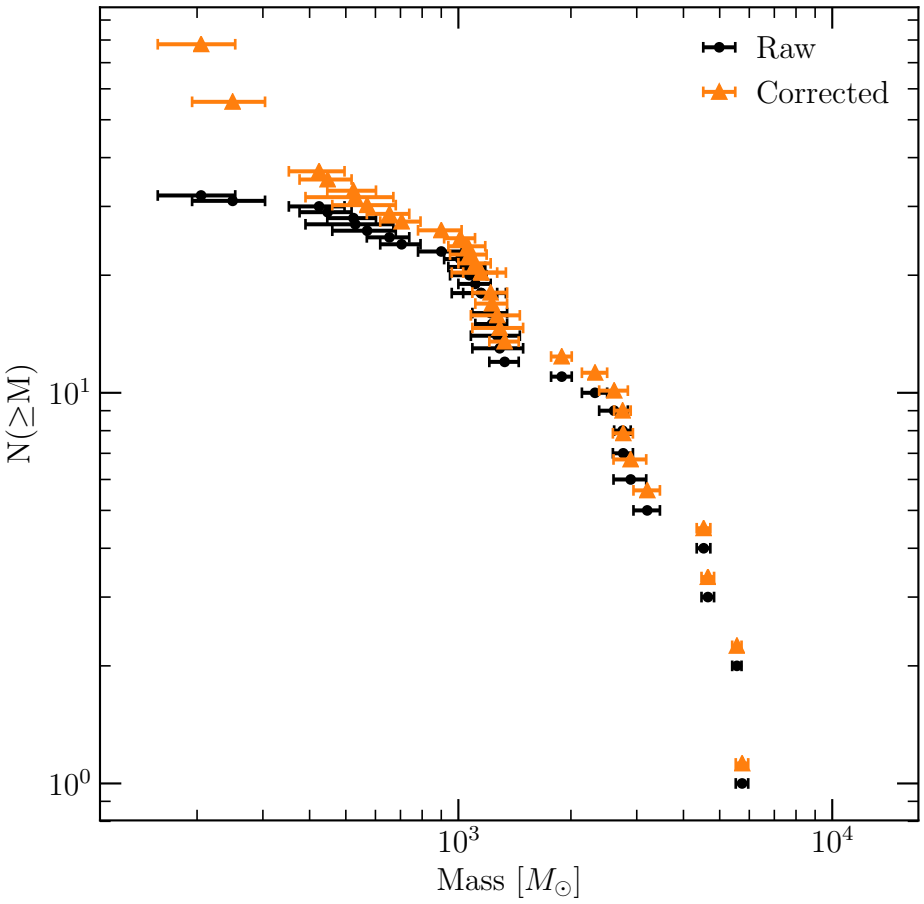

Figure 3.11: Comparison of "raw" and completeness corrected dust-only clump mass functions.

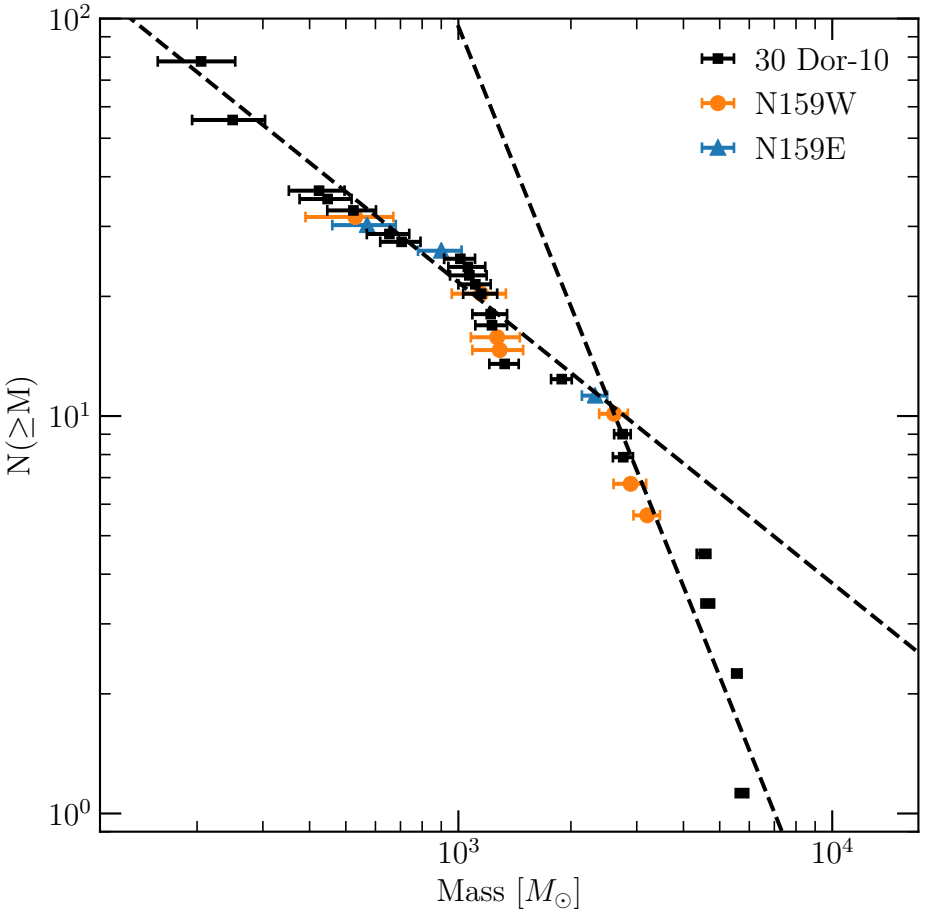

Figure 3.12: Completeness corrected clump mass function with best fit double power law plotted as black dashed lines. Regions from which clumps originate are marked.

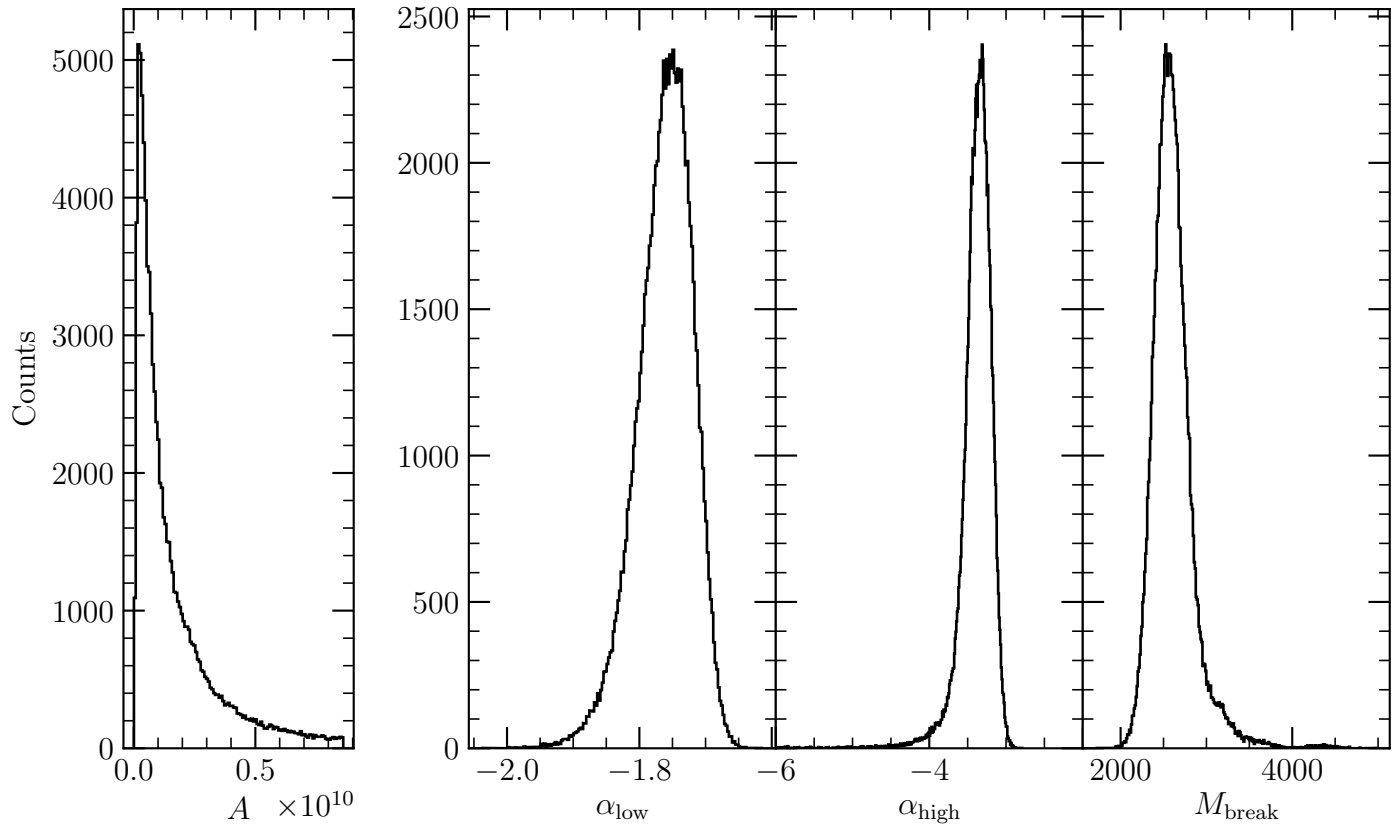

Figure 3.13: Distributions of best fit parameters from 10^5 artificial mass function realizations for clump mass function with completeness correction applied. Amplitude histogram is trimmed above the 90th percentile for ease of plotting.

Chapter 4

Discussion And Conclusions

4.1 Comparison To Other Studies

The sample of 11 core/clump mass functions from 7 different star forming regions analyzed by Reid & Wilson (2006a) is a useful one for comparing our LMC clump mass function to Milky Way mass functions. Those regions included ρ Ophiuchus, Orion B, M8, M17, NGC 7538, W43, and RCW 106. Cores and clumps identified spanned five orders of magnitude up to about $9.9 \times 10^4\,\mathrm{M}_\odot$. Double power law fits for all mass functions were reported with low mass power law indices spanning -1.7 ± 0.2 to -1.2 ± 0.1, high mass indices spanning -3.1 ± 0.8 to -1.8 ± 0.6, and break masses spanning $(0.2 \pm 0.1)\,\mathrm{M}_\odot$ to $(400 \pm 300)\,\mathrm{M}_\odot$.

The LMC low mass power law index α_{low} is consistent within uncertainties with two of the double power law mass function fits of Reid & Wilson (2006a): ρ Oph as measured in 1.3 mm continuum and Orion B as measured by Motte et al. (2001). The remainder of the α_{low} fits are still quite similar, though systematically larger (shallower).

For the high mass index $\alpha_{\rm high}$ our best fit to the LMC mass function is also systematically steeper than about half of the Milky Way regions. The exceptions, where our indices are consistent within uncertainties, are Orion B (as measured by both Motte et al. 2001; Johnstone et al. 2001), M8, and M17 (measured in both 450 µm and 850 µm continuum).

Lastly, the break masses are all significantly smaller than our best fit break mass. The highest break mass from Reid & Wilson (2006a) is from RCW 106; even if we take the high end of the uncertainty range of 700 $M_\odot$ our break mass is still more than 3.5 times larger. This difference is not entirely unexpected however as Reid et al. (2010) showed a correlation between distance and break mass using mass functions derived from synthetic observations of a simulated GMC. This trend can even be seen between the 11 mass functions from Reid & Wilson (2006a) as the break masses increase in step with decreasing spatial resolution.

Our results for the break mass are reasonable given the much greater distance to the clumps in the LMC; however the steeper indices seem counter-intuitive. For a survey of objects at a greater distance we are biased towards brighter and therefore more massive objects, at all scales. However, it seems that we have fewer high mass (or more low mass) clumps than we would expect in comparison to the Galactic mass functions.

Directly comparing the double power law fits is likely the problem. Since our break mass is greater than the individual clump masses for all of the Milky Way objects except for W43 and RCW 106, it is probably more accurate to compare our low mass index to the high mass indices of the clouds from Reid & Wilson (2006a). If we make this comparison shown in Figure 4.2, high mass indices for ρ Oph, Orion B, NGC 7538 W43, and RCW 106 are consistent with

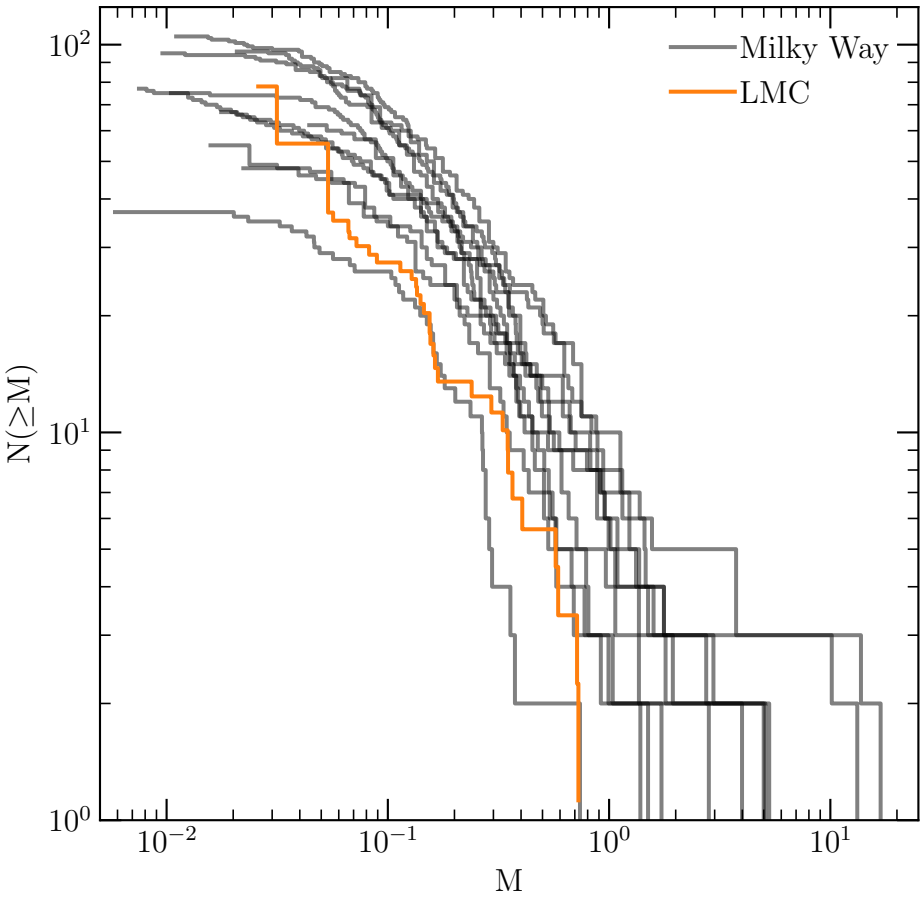

Figure 4.1: All Milky Way mass functions described in Reid & Wilson (2006a) reproduced from their Figure 8 along with our completeness corrected LMC mass function. All masses have been renormalized to have the same median mass.

our low mass index. Figure 4.1 shows this comparison in another way. All mass functions have been renormalized such that they share a common median mass. We show our completeness corrected mass function for the LMC which clearly has a similar shape at low masses to the high mass ends of the Milky Way clouds and a steeper slope at high masses.

Orion B should likely be taken with a grain of salt given its high mass indices are consistent with both of our indices due to relative uncertainties

of almost 50 %. The remaining fields, M8 and M17 challenge this interpretation as their mass ranges are well below ours but their high mass indices are consistent with our high mass index. It should be noted that the M8 cores were identified by eye rather than algorithmically as well as being fit with an assumed Gaussian profile unlike most of the other clump finding, including our own. Also, the mass functions of M17 were either fit as well or better by a log-normal form so it may not be a fair comparison with our mass function if it is not well characterized by a double power law. It could also be that our much steeper high mass index could be consistent with a log-normal mass distribution populating the entire mass range of all of these cores and clumps.

Another interesting comparison we can make is to the clump mass function derived by Indebetouw et al. (2013) from the same 30 Dor-10 project as our continuum data but using the ^{13}CO (2-1) and ^{12}CO (2-1) data. Their fit to the differential form of $dN/d(\log M) \propto M^{\alpha}$ for $M > 500$ M$_{\odot}$ resulted in $\alpha = -0.9 \pm 0.2$. Converting this slope to the cumulative mass function index by subtracting one shows that their power law is consistent with our low mass power law. As their binning results in fitting only about five bins, two of which only have one or two clumps, it seems reasonable that the bins below our break mass would dominate their fit. The similar mass ranges between our dust estimated masses and their independent CO estimated masses is evidence for the accuracy of our dust-only map generation and our estimation of the dust properties.

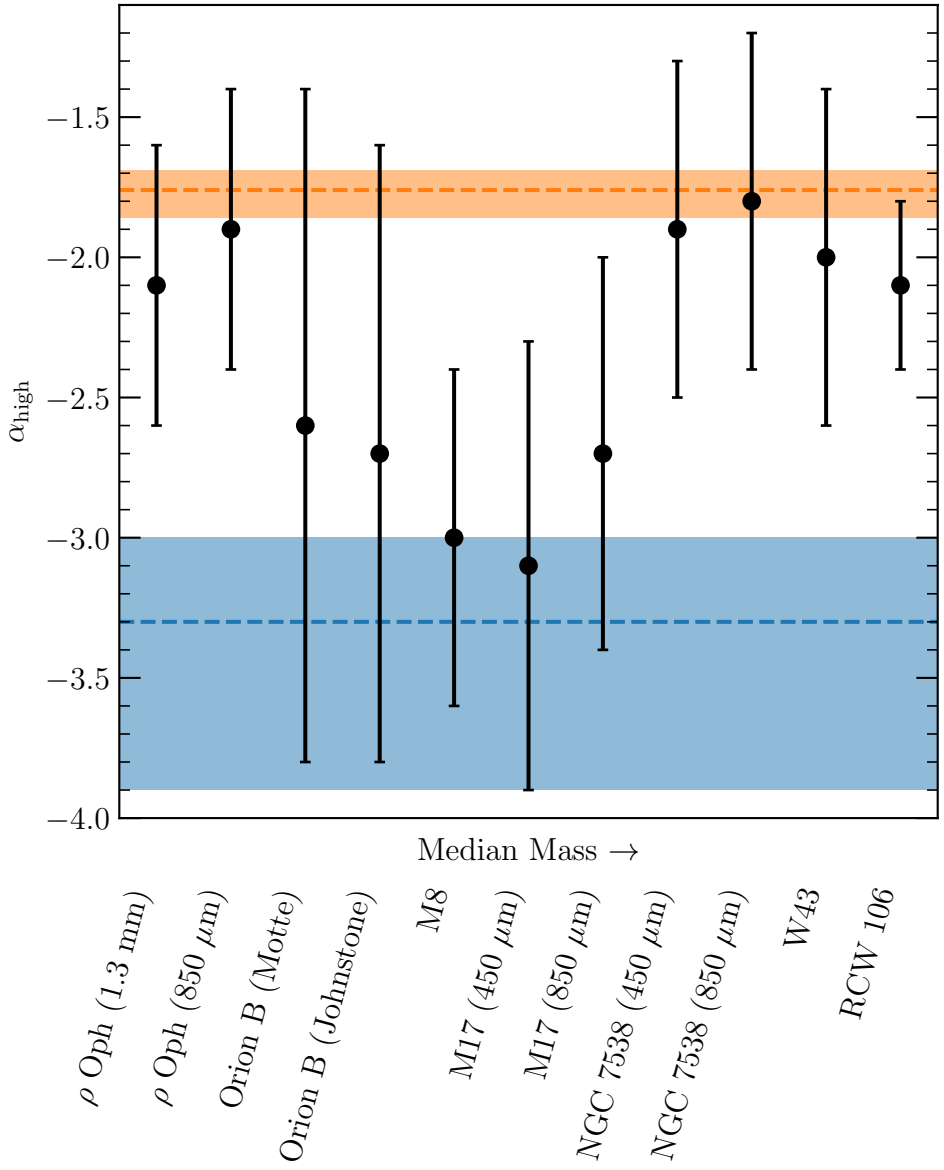

Figure 4.2: Comparison of the high mass power law mass function fits from the seven star forming regions summarized in Reid & Wilson (2006a) with the low and high mass fit indices for our LMC mass function. The orange and blue dashed lines and shaded regions show the low and high mass indices for the LMC, respectively. Milky Way clouds are arranged with their median core/clump masses increasing from left to right.

4.2 Completeness

Regarding our method of estimating completeness there is an important caveat to keep in mind. We only tested source recovery for sources that were the same size as the synthesized beam for those observations. While this means we have a legitimate estimate of the point source recovery rate, most of the clumps we have identified and are analyzing are much larger than the synthesized beam. This is more a general challenge of identifying these types of objects rather than a shortcoming of our method. The molecular clumps are intrinsically amorphous in shape and vary significantly in physical size. The ClumpFind algorithm is built upon those facts as it does not attempt to find objects of a given shape or size (in contrast to other source finding algorithms such as GaussClumps). The consequence of our estimating the completeness in this way is that the actual detected fraction of clumps of some given shape and size (other than the beam shape) is unknown. Pairing this with the fact that larger clumps of the same integrated flux density as smaller clumps have lower S/N means our completeness estimates are likely overestimating the total fraction of clumps recovered for a given mass. As a result, the power law indices of our mass function should likely be taken as upper limits to the true index as additional missing sources would still affect the lower masses most. While more sophisticated methods can be employed (e.g. see Appendix B of Könyves et al. 2015) having even a simplistic estimate of the completeness is essential for interpreting these types of results.

An initially unexpected outcome from our completeness testing was that none of the maps actually attains 100 % completeness for our point source recovery. A clue to the cause is in the trend of increasing maximum complete-

ness with less crowded maps. The least crowded field N159E reaches about 97 % completeness while the much more crowded map of 30 Dor-10 asymptotes around 89 % complete, with the intermediate field N159W around 95 %. This trend indicates that not only the noise and resolution but also the crowdedness of our maps are limiting our ability to find clumps. The obvious situation is when a synthetic source is placed in the map that it lands on top of a clump that was identified in the original clump finding so that ClumpFind does not see an extra clump.

Not only does crowding reduce the maximum completeness of the map but it also acts to broaden the middle mass range of the completeness curve. This effect is also most pronounced for 30 Dor-10, least for N159E, and intermediate for N159W. Luckily, while crowding can cause the mass for a given completeness to be shifted higher, 30 Dor-10 has the highest intrinsic sensitivity of the three regions.

One more subtle consequence of the crowdedness of the maps is really only seen in 30 Dor-10 and N159W. After the completeness curves flatten out at the high mass end they actually begin to trend downwards in recovery rate for higher masses. Somehow the highest mass synthetic sources are not the easiest to recover. The different color curves shown in Figure 3.8 shows what is happening. During our completeness testing we chose to count when the same number of clumps as the original clump finding were found, fewer than the original, and more than the original. The orange curves show the fraction of tests where less than the original number of clumps were found and this only begins to be appreciable at the highest masses when the completeness begins trending downwards. This is showing that when a very bright synthetic source overlapped with clumps identified in the original map they actually

caused real clumps to merge. We see this happening in the actual data when we compare the Band 6 and dust mass functions in Section 4.3. There we can see the blending was occurring because Band 6 clumps sometimes break into multiple dust clumps after free-free correction.

4.3 Other Data

Since almost half of the fields we investigated from the archive were continuum non-detections this raises the question of whether those data are inherently of poorer sensitivity compared to the data that has abundant emission. The most straightforward comparison would be to simply measure the RMS of emission-free regions in all of the maps. The surface brightness units of Jy/beam that the images are made in however means the comparison could not be measured directly in the maps we had produced in Figures 2.5 to 2.10. We needed to match the beams of all maps so that the per beam part of the surface brightnesses would be the same. As we did before for matching the resolution between bands of the same region, we did an inner UV trimming and tapered the maps to a common resolution and then we measured the RMS noise in the output maps. All common beam maps were made with the same setting of `robust=0.5` for as direct a comparison as possible and Table 4.1 lists the results. Interestingly, the non-detection maps do not show dramatically higher noise at these scales and in Band 3 they even have the lowest noise. This instead points to differences in the physical densities and sizes of the emitting sources in the two bands. If Band 3 is truly dominated by free-free emission then this could be showing that GMC 225 and N166 are lacking in compact sources of ionized gas and thus have fewer or younger HII regions. For PCC

Table 4.1: Sensitivities for all fields matched to common beams.

Field Name	3.1 mm RMS[a] (μJy/beam)	1.3 mm RMS[b] (μJy/beam)
30 Dor-10	962	377
N159W	1310	383
N159E	575	419
N113	...	403
GMC 225	193	804
N166	216	1000
PCC 11546	...	213

NOTE.—Common beams were determined by the largest of each axis across all fields. Some small padding was necessary to make sure the data with the largest beam dimension could still be tapered along the other axis to match the full common beam size. This means the common beams are slightly larger in both dimensions than the maximum major and minor beam axes.

[a] Common beam was $3.8'' \times 3.0''$. Maximum major axis was taken from GMC 225 ($3.71''$) and maximum minor axis from N166 ($2.93''$). Minimum baseline was 2781.61 λ from N159W.

[b] Common beam was $1.94'' \times 1.28''$. Maximum major and minor axes are from 30 Dor-10. Minimum baseline was 8665.29 λ from N113.

11546 this would mean the same thing but for compact dust emission. A key caveat with that statement is that we can only speak to the compact spatial scales the interferometer is sensitive to as it only provides information on a range of scales. If GMC 225, N166, and PCC 11546 are relatively more diffuse than the other fields and are therefore only emitting on scales larger than the interferometer is sensitive to then the regions could be booming at these frequencies but we would not pick up that emission.

Since we chose to estimate the dust-only emission in the data we retrieved from the archive it meant that we could not incorporate N113 into the final mass function and analysis. Without a Band 3 measurement we could not directly remove the free-free contamination. We originally chose to include N113 in the sample to help boost the sample size but the evidence for free-free

contamination showed that Band 6 observations alone would not produce an accurate clump mass function. The same rationale was used for choosing to include PCC 11546, especially considering the large area of the sky that was mapped. Not being able to include N113 was unfortunate since it contributed about the same number of clumps as the N159E Band 6 map but over a much smaller area. Possible ways to incorporate the Band 6 only observations of N113 are discussed in the next section.

Comparing the Band 6 clump mass function and the dust-only clump mass function (as in Figure 3.6) gives us a first order check of our free-free removal. The distribution shifts to lower masses when the free-free contamination is removed which is consistent with the goal of removing additional emission that is not coming from dust. Since the masses are proportional to the integrated flux densities of the clumps the masses should be lower when flux is subtracted.

The total number of clumps also changes from the Band 6 to the dust-only mass function. Figure 3.6 shows clumps from the same fields in both mass functions, i.e. only 30 Dor-10, N159W, and N159E. The difference in numbers comes from three things happening. Some larger clumps in Band 6 are actually dominated by HII regions with a large portion of free-free emission. When the ionized gas emission is removed a hole is left around which dust clumps are still present. So a large Band 6 clump can break up to reveal a small group of dust clumps. N159E exhibits this effect with its brightest Band 6 clump. This effect alone cannot explain the change in clump numbers however because there are fewer dust-only than Band 6 clumps, not more. The next scenario has clumps being subtracted to below the clump finding threshold as they were predominantly free-free emission. The isolated clumps in the southern part of the N159E maps are a good example of this where the ratio of emission in the

two bands is such that the clumps are effectively non-existent in the dust map. Another possibility is that through free-free subtraction the emission became smooth enough that multiple clumps are merged into fewer spatially larger clumps by ClumpFind. This happened primarily for the faint filament in the southeast portion of the 30 Dor-10 maps.

4.4 Future Work

Several extensions of this work are interesting routes to further investigate the mass function of clumps in the LMC. The first builds from the discussion in the previous section about the observations that only contain Band 6 data. Being able to incorporate Band 6 maps alone would widen the possible data sets available and likely increase the sample of clumps. Investigating a statistical approach to correcting for free-free contamination in Band 6 observations could be a step in that direction. Identifying an average correction factor for Band 6 identified clumps based on clumps identified with both Band 3 and 6 observations may be possible, especially if more fields can be added so that regions of similar properties such as temperature and density can be matched. There may be too much variation in those properties among the current sample of clouds but if the number of clumps can be built up for more similar regions then the uncertainty in applying an aggregate correction could be reduced. The primary drawback of this approach is that we would be uncertain of the true spatial variation of the different sources of emission. The way the main HII region in the Band 6 observations of N159E breaks into several surrounding dust clumps in the dust-only map is a good example of this. Not only could clump numbers be underestimated in that scenario but there are

sometimes clumps that are entirely absent in the dust-only map despite being present in both bands.

Being able to quantify the quality of our free-free removal would be another powerful next step. Continuum observations of star forming regions in ALMA's Band 7 (centered near 325 GHz or 1 mm) could be used to measure the blackbody emission of the cold dust more directly. If used in combination with Bands 3 and 6 then a simple SED could be modeled for the region, giving a better handle on the different components of emission. This SED model could then be compared to the dust emission estimated using our algebraic combination of the Band 3 and 6 observations. While it would be ideal to have three band observations for all regions, we could carry out this SED analysis on even a few regions, then we could use what we find to improve the Bands 3 and 6 method in other regions. If our method of free-free correction can be confirmed to be relatively accurate then it could provide an alternative means of measuring dust masses with observations that are less impacted by poorer weather than Band 7.

The low frequency end of the spectrum would be better at constraining the synchrotron emission in these regions. A better estimate of synchrotron emission through observations at lower frequencies would give us a handle on how accurate our assumption is that Band 3 observations are dominated by free-free emission. This check could allow for making dust-only measurements that were devoid of free-free and synchrotron emission.

Simply obtaining observations of more star forming clouds is also a natural extension. Building the sample size of clouds in the LMC would not only allow us to better determine a global clump mass function but possibly to begin breaking the sample up to make comparisons between different fields in the

LMC itself. Testing the universality of our findings in the LMC is necessary for understanding whether our findings here have revealed something intrinsic about the system or are merely a consequence of the particular assortment of data to which we had access. New observations should be targeted primarily at regions that are likely to host significant compact molecular cloud structure to maximize the yield of clumps with ALMA. Abundant molecular gas should mean those types of regions would also be relatively bright as a consequence. Higher levels of emission could mean shorter integration times to obtain useful results and would allow for proposals covering larger regions. Efficiently optimizing the return for the area observed is essential for an instrument like ALMA whose real strength of carefully dissecting small portions of the sky can potentially hinder the growth of the clump sample size. Continuing to use newly public archival observations would be a straightforward way to add to the clump sample.

As the sample size is increased it should be possible to better estimate the appropriate fitting function for these mass functions. Even before more clumps can be added to this sample it would be worthwhile to examine the ability of the log-normal form to reproduce our mass function results. The LMC mass function does appear to possibly have a smoother rollover than the stitching together of two power laws would indicate. Having a statistical comparison of our double power law fit to a log-normal fit would help in comparisons to other fields as well. If the mass functions from different regions are not well represented by power laws then there likely would not be very much useful information to gather from comparing fits that do not represent the intrinsic shape of those mass functions.

A way in which our results can be verified with data that already exists is

through the analysis of the spectral line observations that accompany all of the continuum observations shown here. Clumps can be identified in the molecular line observations in a similar way as they are in continuum data but with the addition of searching along the third, spectral axis. This tends to increase the complexity of source extraction but with the benefit of making it possible to distinguish clumps along the line of sight that appear superimposed on the plane of the sky. Total clump masses can be estimated from the spectral line observations in a way that is complementary to the method used with continuum observations. Matching clumps spatially between continuum and spectral line observations and then comparing the estimated masses offers a verification of the masses through independent measurements. The kinematic information that is often available from spectral line data could also enable an analysis of the gravitational boundedness of the clumps in these mass functions. Being able to pick out clumps that are most likely collapsing gravitationally from the ones that are simply transient structures appearing in these regions would more accurately represent the population of star forming clumps.

4.5 Summary

We have presented a clump mass function measured in dust continuum emission from star forming molecular clouds in the LMC derived from public archival ALMA observations. Clumps were observed in the 30 Dor-10, N159W, and N159E regions with masses ranging between 205 $M_\odot$ and 5740 $M_\odot$. To derive these total masses from the thermal dust emission we presented a technique of combining Band 3 and 6 maps to remove free-free emission contamination and produce dust-only emission maps. We have also described and presented

the automatic masking script we used in cleaning all of the maps presented here.

From our clump mass function we derived a double power law best fit with parameters $\alpha_{\rm low} = -1.76^{+0.07}_{-0.1}$, $\alpha_{\rm high} = -3.3^{+0.3}_{-0.6}$, and $M_{\rm break} = 2500^{+700}_{-300}$ $M_\odot$. Our low mass power law index is similar to the high mass indices of Milky Way regions hosting smaller mass cores and clumps. This may indicate an extension of the Milky Way power law to higher masses. The addition of more clumps from more regions in the LMC along with mass functions derived from spectral line emission will be necessary to better characterize the mass distribution of these objects in the LMC and to investigate its consistency with the Milky Way mass functions.

Technical Acknowledgments

This thesis makes use of the following ALMA data:

- ADS/JAO.ALMA#2011.0.00471.S,
- ADS/JAO.ALMA#2012.1.00554.S,
- ADS/JAO.ALMA#2012.1.00603.S,
- ADS/JAO.ALMA#2013.1.00832.S,
- ADS/JAO.ALMA#2013.1.01091.S,
- ADS/JAO.ALMA#2013.1.01136.S, and
- ADS/JAO.ALMA#2016.1.01533.S.

ALMA is a partnership of ESO (representing its member states), NSF (USA) and NINS (Japan), together with NRC (Canada), MOST and ASIAA (Taiwan), and KASI (Republic of Korea), in cooperation with the Republic of Chile. The Joint ALMA Observatory is operated by ESO, AUI/NRAO and NAOJ. The National Radio Astronomy Observatory is a facility of the National Science Foundation operated under cooperative agreement by Associated Universities, Inc.

This research has made use of NASA's Astrophysics Data System Bibliographic Services.

This research made use of Astropy, a community-developed core Python package for Astronomy (Astropy Collaboration, 2013).

This research made use of APLpy, an open-source plotting package for Python (Robitaille and Bressert, 2012).

This thesis was typeset using the LaTeX typesetting system originally developed by Leslie Lamport, based on TeX created by Donald Knuth.

Bibliography

Alves, J., Lombardi, M., & Lada, C. J. 2007, A&A, 462, L17

André, P., Men'shchikov, A., Bontemps, S., et al. 2010, A&A, 518, L102

André, P., Revéret, V., Könyves, V., et al. 2016, A&A, 592, A54

Arzoumanian, D., André, P., Didelon, P., et al. 2011, A&A, 529, L6

Berry, D. S., Reinhold, K., Jenness, T., & Economou, F. 2007, in Astronomical Society of the Pacific Conference Series, Vol. 376, Astronomical Data Analysis Software and Systems XVI, ed. R. A. Shaw, F. Hill, & D. J. Bell, 425

Bica, E., Claria, J. J., & Dottori, H. 1992, AJ, 103, 1859

Briggs, D. S. 1995, in Bulletin of the American Astronomical Society, Vol. 27, American Astronomical Society Meeting Abstracts, 1444

Bromm, V. 2005, in Astrophysics and Space Science Library, Vol. 327, The Initial Mass Function 50 Years Later, ed. E. Corbelli, F. Palla, & H. Zinnecker, 469

Chabrier, G. 2003, PASP, 115, 763

Chabrier, G. 2005, in Astrophysics and Space Science Library, Vol. 327, The Initial Mass Function 50 Years Later, ed. E. Corbelli, F. Palla, & H. Zinnecker, 41

Chabrier, G., & Hennebelle, P. 2010, ApJL, 725, L79

Currie, M. J., Berry, D. S., Jenness, T., et al. 2014, in Astronomical Society of the Pacific Conference Series, Vol. 485, Astronomical Data Analysis Software and Systems XXIII, ed. N. Manset & P. Forshay, 391

De Becker, M., & Raucq, F. 2013, A&A, 558, A28

De Marchi, G., Paresce, F., Panagia, N., et al. 2011, ApJ, 739, 27

Dufour, R. J. 1984, in IAU Symposium, Vol. 108, Structure and Evolution of the Magellanic Clouds, ed. S. van den Bergh & K. S. D. de Boer, 353–360

Fall, S. M., & Chandar, R. 2012, ApJ, 752, 96

Freeman, P., Rosolowsky, E., Kruijssen, J. M. D., Bastian, N., & Adamo, A. 2017, MNRAS, 468, 1769

Fujii, K., Minamidani, T., Mizuno, N., et al. 2014, ApJ, 796, 123

Fujii, M. S., & Portegies Zwart, S. 2015, MNRAS, 449, 726

Fukui, Y., Mizuno, N., Yamaguchi, R., Mizuno, A., & Onishi, T. 2001, PASJ, 53, L41

Fukui, Y., Mizuno, N., Yamaguchi, R., et al. 1999, PASJ, 51, 745

Fukui, Y., Kawamura, A., Minamidani, T., et al. 2008, ApJS, 178, 56

Fukui, Y., Harada, R., Tokuda, K., et al. 2015, ApJL, 807, L4

Ginsburg, A., Goss, W. M., Goddi, C., et al. 2016, A&A, 595, A27

Gordon, K. D., Roman-Duval, J., Bot, C., et al. 2014, ApJ, 797, 85

Guszejnov, D., & Hopkins, P. F. 2015, MNRAS, 450, 4137

Harris, W. E., Blakeslee, J. P., Whitmore, B. C., et al. 2016, ApJ, 817, 58

Henize, K. G. 1956, ApJS, 2, 315

Hill, T., André, P., Arzoumanian, D., et al. 2012, A&A, 548, L6

Howard, C. S., Pudritz, R. E., & Harris, W. E. 2017, MNRAS, 470, 3346

Hughes, A., Wong, T., Ott, J., et al. 2010, MNRAS, 406, 2065

Hunter, D. A., Shaya, E. J., Holtzman, J. A., et al. 1995, ApJ, 448, 179

Imai, H., Katayama, Y., Ellingsen, S. P., & Hagiwara, Y. 2013, MNRAS, 432, L16

Indebetouw, R., Brogan, C., Chen, C.-H. R., et al. 2013, ApJ, 774, 73

Johansson, L. E. B., Greve, A., Booth, R. S., et al. 1998, A&A, 331, 857

Johnstone, D., Fich, M., Mitchell, G. F., & Moriarty-Schieven, G. 2001, ApJ, 559, 307

Jones, E., Oliphant, T., Peterson, P., et al. 2001–, SciPy: Open source scientific tools for Python, [Online; accessed 2017-03-17]. `http://www.scipy.org/`

Kawamura, A., Mizuno, Y., Minamidani, T., et al. 2009, ApJS, 184, 1

Könyves, V., André, P., Men'shchikov, A., et al. 2015, A&A, 584, A91

Krumholz, M. R. 2014, PhR, 539, 49

Lada, C. J., & Lada, E. A. 2003, ARA&A, 41, 57

Lada, E. A. 1992, ApJL, 393, L25

Lada, E. A., Bally, J., & Stark, A. A. 1991a, ApJ, 368, 432

Lada, E. A., Depoy, D. L., Evans, II, N. J., & Gatley, I. 1991b, ApJ, 371, 171

Massey, P., & Hunter, D. A. 1998, ApJ, 493, 180

McMullin, J. P., Waters, B., Schiebel, D., Young, W., & Golap, K. 2007, in Astronomical Society of the Pacific Conference Series, Vol. 376, Astronomical Data Analysis Software and Systems XVI, ed. R. A. Shaw, F. Hill, & D. J. Bell, 127

Meixner, M., Panuzzo, P., Roman-Duval, J., et al. 2013, AJ, 146, 62

Mizuno, N., Rubio, M., Mizuno, A., et al. 2001, PASJ, 53, L45

Mizuno, Y., Kawamura, A., Onishi, T., et al. 2010, PASJ, 62, 51

More, J. 1977, Levenberg–Marquardt algorithm: implementation and theory. http://www.osti.gov/scitech/servlets/purl/7256021

Motte, F., André, P., Ward-Thompson, D., & Bontemps, S. 2001, A&A, 372, L41

Netterfield, C. B., Ade, P. A. R., Bock, J. J., et al. 2009, ApJ, 707, 1824

Paron, S., Ortega, M. E., Cunningham, M., et al. 2014, A&A, 572, A56

Paron, S., Ortega, M. E., Fariña, C., et al. 2016, MNRAS, 455, 518

Pattle, K., Ward-Thompson, D., Kirk, J. M., et al. 2017, MNRAS, 464, 4255

Pietrzyński, G., Graczyk, D., Gieren, W., et al. 2013, Nature, 495, 76

Planck Collaboration, Ade, P. A. R., Aghanim, N., et al. 2016, A&A, 594, A28

Reid, M. A., Wadsley, J., Petitclerc, N., & Sills, A. 2010, ApJ, 719, 561

Reid, M. A., & Wilson, C. D. 2005, ApJ, 625, 891

—. 2006a, ApJ, 650, 970

—. 2006b, ApJ, 644, 990

Rolleston, W. R. J., Trundle, C., & Dufton, P. L. 2002, A&A, 396, 53

Roman-Duval, J., Bot, C., Chastenet, J., & Gordon, K. 2017, ApJ, 841, 72

Rosolowsky, E., & Leroy, A. 2006, PASP, 118, 590

Rubio, M., Elmegreen, B. G., Hunter, D. A., et al. 2015, Nature, 525, 218

Saigo, K., Onishi, T., Nayak, O., et al. 2017, ApJ, 835, 108

Salpeter, E. E. 1955, ApJ, 121, 161

Schruba, A., Leroy, A. K., Kruijssen, J. M. D., et al. 2017, ApJ, 835, 278

Seale, J. P., Looney, L. W., Wong, T., et al. 2012, ApJ, 751, 42

Selman, F. J., & Melnick, J. 2013, A&A, 552, A94

Staveley-Smith, L., Kim, S., Calabretta, M. R., Haynes, R. F., & Kesteven, M. J. 2003, MNRAS, 339, 87

van der Marel, R. P., Alves, D. R., Hardy, E., & Suntzeff, N. B. 2002, AJ, 124, 2639

Walborn, N. R., & Blades, J. C. 1987, ApJL, 323, L65

Wang, K., Testi, L., Burkert, A., et al. 2016, ApJS, 226, 9

Ward, J. L., Oliveira, J. M., van Loon, J. T., & Sewiło, M. 2016, MNRAS, 455, 2345

Williams, J. P., de Geus, E. J., & Blitz, L. 1994, ApJ, 428, 693

Wong, T., Hughes, A., Ott, J., et al. 2011, ApJS, 197, 16

Wong, T., Hughes, A., Tokuda, K., et al. 2017, ArXiv e-prints, arXiv:1708.08890

Appendix A

Interferometric Imaging And The `clean` Algorithm

We give a brief (and simplified) description of interferometric imaging and the `clean` algorithm to help clarify the various beams and imaging weightings discussed throughout this thesis. The calibrated science source visibilities (effectively the amplitudes and phases of the interference fringes) can be placed on a uniform grid, Fourier transformed and cleaned to produce an image of the sky. The gridding allows for the use of the discretized Fast Fourier Transform and it is at this step that imaging weighting can be applied. These weights can accentuate different aspects of the spatial distribution of the visibilities. For example, long baseline visibilities can be up-weighted to produce images that accentuate the high spatial frequency (high resolution) features of the field. Often this is accompanied with increased noise due to down-weighting the (short baseline) visibilities which most completely sample the UV plane. The opposite weighting scheme can be applied, producing images that have lower noise but some of the highest resolution information washed out. This

trade off is what we experimented with for the non-detection fields to boost their S/N as discussed in Section 4.3.

With radio interferometric observations it is possible to produce a map of the array's point source response pattern, or dirty beam. The positions of the antennas are set in the UV plane, amplitudes of one and phases of zero are assigned to each antenna visibility and this UV distribution is gridded and Fourier transformed to produce the dirty beam map. The dirty beam contains artifacts of the incompletely sampled UV plane which have nothing to do with the emission from the source, hence the "dirty" in the name.

Somewhat similarly, a dirty map of the actual science field can be created but instead by Fourier transforming the calibrated science observation visibilities. This is called the dirty map because it is the distribution of emission on the sky convolved with the array's dirty beam. The imprint of the dirty beam on the true sky emission distribution can be reduced by defining a "clean" beam shape which excludes most of the artifacts brought on by the arrangement of the antennas. The standard implementation of the `clean` algorithm in CASA assumes that the point source response would be a Gaussian of the same size and orientation as the inner-most part of the dirty beam. So in CASA the clean beam is a 2D elliptical Gaussian fit to the central portion of the dirty beam.

Attempting to reconstruct the true distribution of the emission on the sky from the dirty map is where the `clean` algorithm steps in. The process starts by identifying the brightest pixel in the dirty map and placing a copy of it in a blank copy of the dirty map. This new map is the emission model map where point sources are used to model the dirty map. Next, that brightest pixel is convolved with the dirty beam and subtracted from the original dirty

map, effectively removing that pixel's emission. In practice, only a fraction of the brightest pixel is convolved and subtracted in each step, to improve the stability of the algorithm. Then the next brightest pixel is identified, placed in the model map, convolved (alone) with the dirty beam and subtracted from the (already once-subtracted) dirty map. As this process is repeated many times, the model map is populated with point sources that, when convolved with the dirty beam, reproduce the observed dirty map, and a residual map with (ideally) all of the emission "cleaned" out leaving just the instrumental noise.

The final steps are convolving the model map of point source pixels with the *clean* beam to produce a noiseless model of the sky emission, and adding the residual noise map to this noiseless model map. This combination of the model map convolved with clean beam plus the residual map is the cleaned map. For most algorithms the model pixels are actually stored as synthetic visibilities back in the UV plane and the dirty source subtraction is done in the UV plane as well.

Appendix B

Automatic `clean` Masking

To efficiently approach the task of masking the complex regions of emission in 30 Dor-10 and to create a reproducible procedure for cleaning all of the fields in this work we adopted an automatic thresholding algorithm. To simplify its use on multiple fields we put together a more user-friendly CASA script which simplifies inputting all of the necessary parameters and running all of the code. The algorithm at the heart of our auto-masking script is from the M100 CASA Guide[1] as it was in August, 2016. As there are not yet any auto-masking utilities in wide use by the community, we describe the main process of the algorithm here and provide the code as we used it to clean the maps included in this thesis.

B.1 Algorithm

The algorithm works iteratively to build up mask regions around emission through multiple steps of thresholding and includes not only a check for the

[1]The M100 CASA Guide was accessed at `https://casaguides.nrao.edu/index.php/M100_Band3_Combine_4.3`.

significance of the emission but also for the size of isolated mask regions. This is done so that only portions of the maps containing obvious emission are masked for cleaning and that mask regions that are too small compared to the synthesized beam of the observations are rejected as likely spurious noise peaks. Inputs to the script are any standard `clean` parameters along with a stopping intensity threshold, a minimum size to accept isolated mask regions and a CASA region text file (CRTF) specifying an emission-free portion of the dirty map.

The actual steps of the auto-masking are as follows. A dirty map is made and the input region (specified by the CRTF) is used to measure the RMS in the map. The peak value in the dirty map is then recorded and the first threshold above which pixels are to be included in the first mask is set to 1/4 of the peak. From the array of pixels above that threshold, isolated regions that are smaller in area than the synthesized beam times an input factor (0.5 in all of our cleaning) are removed and the remaining pixels become the `clean` mask. This same masking threshold is then fed into `clean` as the `threshold` parameter along with the automatically generated mask and cleaning is done non-interactively. Once cleaning is complete, the initial threshold is halved and the process is repeated starting with finding pixels in the residual map above the threshold to consider for a new mask.

The cycle is repeated until the current iteration threshold is less than the input stopping threshold. If the `restoringbeam` `clean` parameter was given to the script, it is used only in the final `clean` call of the final auto-masking iteration. This causes all cleaning to be done at the intrinsic resolution of the data and only in the very last step is the model map convolved to the desired clean beam resolution. We used the `restoringbeam` parameter with

the auto-masking script when imaging the Band 6 data to exactly match the resolution to the Band 3 maps. Our script is currently only designed for use on single-plane continuum images but the original CASA Guide code was able to work on image cubes as well.

Starting with masks thresholded at a considerable fraction of the peak in the dirty map should make sure the initial mask is only cleaning what is certainly emission. As the emission is cleaned and subtracted away and the mask is expanded by lowering the mask threshold, the lower-lying emission should be slowly incorporated into the masks and cleaned (see Figure B.1). Picking a sensible stopping threshold is still very important as the algorithm will happily clean down into the noise, picking out false peaks and incorrectly redistributing flux in the map. For this work, we found that stopping thresholds of 1.5 to 3 times the RMS noise usually cleaned most of the brightest emission without the mask trying to include too much of the noise. Excluding noise peaks is also somewhat mitigated by the inclusion of a check on the size of an isolated mask region against the input minimum acceptable size.

To be clear, this auto-masking script does not automatically find the optimal parameters with which to clean a map. It will simply take a lowest threshold to clean down to based on the RMS in an input region and a minimum spatial scale to throw out masks that are deemed too small. Careful inspection of the final maps produced is absolutely necessary and was carried out on each field in each band. In particular, we recommend three general spot-checks to ensure the script worked as expected:

- check the residual maps to see if the main emission regions look mostly like the noise in regions around them (i.e. not excessively flat from too

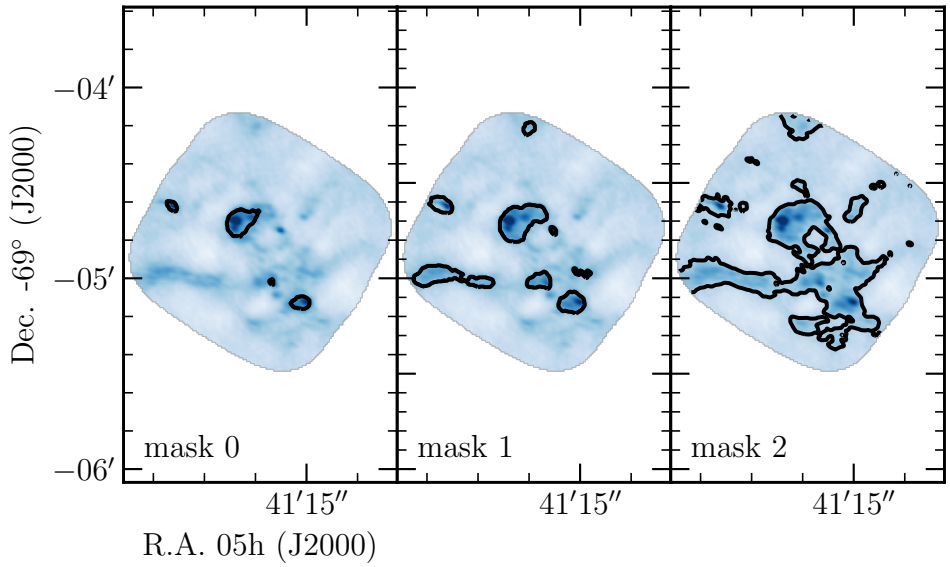

Figure B.1: Progression of mask at several steps of the auto-masking procedure as lower-level emission regions are incorporated into the overall mask. Black contours show extent of masks and background color map is the resulting cleaned Band 6 map for 30 Dor-10.

much cleaning);

- increase the stretch on the final cleaned maps to look for obvious artifacts from unflagged bad data or cleaning noisy regions; and
- look at the final mask built in the auto-masking to make sure it follows where there was obvious emission and was not including small regions that were likely just noise peaks.

Following these rough steps allowed us to find what should be optimal (and reproducible) cleaning parameters, similar to if we had interactively built the masks and cleaned the images.

Another noteworthy test was to see if there was a difference in the final cleaned map when building up the mask through multiple `clean` calls, as done with this script, or simply cleaning all at once with the final mask. We tested

this by running the script to clean N159W in Band 3 which produces the final map used in this thesis. Then we took the final mask from the auto-masking script, which should encompass all the emission of the field, and fed it into `clean` to start fresh from the dirty map. Comparing maps showed they were extremely similar, with a peak difference of 10^{-4} Jy/beam and an RMS of the difference map of 2×10^{-5} Jy/beam.

B.2 CASA Script

```
"""
Tool to non-interactively image and CLEAN
visibilities with iteratively improved and
automatically generated CLEAN masks. Basic process is
    1. a dirty map is made
    2. you give this script a CASA region text file
       (CRTF) from the viewer to estimate the RMS in
       that dirty map
    3. you specify a stopping criteria as a multiple
       of that RMS
    4. masks are made where pixels are above that
       stopping criteria as well as being within the
       specified minimum primary beam region and not
       being smaller than a specified multiple of the
       synthesized beam area
    5. an initial CLEAN threshold is set to a
       fraction of the dirty map peak
```

```
    6. the map is cumulatively CLEANed with the
       latest mask and current CLEAN threshold
    7. the CLEAN threshold is halved
    8. repeat steps 6 and 7 until the CLEAN threshold
       is less than the specified stopping criteria
It must be run within CASA as it uses multiple tasks.

There are two ways of running this script.
    1. Edit the parameters under the 'initialize
       CLEAN parameters' and 'stuff related to
       auto-masking' comments in this file and then
       run
         $ casa --nologger --nogui -c
            auto_mask_CLEANing.py
       in a terminal.
    2. Start an instance of CASA (DO NOT include the
       --nologger and --nogui startup options), enter
       each variable definition for the user defined
       parameters at the CASA prompt and then run
       this script with execfile
         CASA <1>: execfile('auto_mask_CLEANing.py')
       The user defined parameters saved in this file
       will be completely ignored when running it
       like this.
```

```
This was originally written using CASA 4.6.0-REL
(r36590).
"""
# if makemask path bug is ever fixed can get rid of
# directory changing back and forth along with
# os.path.basename stuff in makemask call

import numpy as np
import os
import scipy.ndimage as sni
import sys

# if running from outside of CASA CLI
if 'casapy.py' not in sys.argv[-1]:
    # intialize CLEAN parameters
    vis = '/home/brunettn/ALMA_archive/' \
          + 'continuum_imaging/2012.1.00554.S/' \
          + 'imaging_N159W/imaging_b3/' \
          + 'averaged_continuum.ms'
    cleanDir = '/home/brunettn/ALMA_archive/' \
               + 'continuum_imaging/' \
               + '2012.1.00554.S/imaging_N159W/' \
               + 'imaging_b3/tst_auto_masking/'
    preName = cleanDir + 'auto_mask_1p5rms_cont'
    field = '0~13'
```

```
    antenna = ''
    phasecenter = 10
    mode = 'mfs'
    psfmode = 'clark'
    cell = '0.21arcsec'
    imsize = 1500
    weighting = 'briggs'
    robust = 0.5
    imagermode = 'mosaic'
    uvrange = '>8022.89lambda'
    uvtaper = False
    outertaper = []
    finalBeam = []
    cyclefactor = 1.5

    # stuff related to auto-masking
    stop = 1.5
    beamMin = 0.5
    rmsCRTF = ''

# CLEAN output names
myImage = preName + '.image'
myFlux = preName + '.flux'
myMask = preName + '.mask'
myResidual = preName + '.residual'
```

```
# change directory to workaround makemask failing
# when specifying paths
origDir = os.getcwd()
os.chdir(cleanDir)

# make dirty image to build first mask from
clean(vis=vis,
      imagename=preName,
      field=field,
      antenna=antenna,
      phasecenter=phasecenter,
      mode=mode,
      psfmode=psfmode
      cell=cell,
      imsize=imsize,
      weighting=weighting,
      robust=robust,
      imagermode=imagermode,
      uvrange=uvrange,
      uvtaper=uvtaper,
      outertaper=outertaper,
      niter=0,
      threshold='0.0Jy',
      cyclefactor=cyclefactor,
```

```
        minpb=minpb,
        interactive=False)

# tell user to go make a CRTF to estimate the RMS in
# the dirty map
if rmsCRTF == '':
    done = False
    rmsCRTF = raw_input('Go draw and save a CASA'
                        +'viewer region for '
                        +'estimating the RMS in the '
                        +'dirty image \n'+myImage
                        +'.\nEnter the full path to'
                        +'that CRTF and press '
                        +'return.\n')
    while not done:
        if not os.path.exists(rmsCRTF):
            rmsCRTF = raw_input(rmsCRTF+' does not'
                                +'exist, try again.'
                                +'\n')
        else:
            print rmsCRTF, 'successfully found.', \
                  'Continuing...'
        done = True
rms = imstat(imagename=myImage,
             region=rmsCRTF)['rms'][0]
```

```
# grab some details from the dirty image
major = imhead(imagename=myImage, mode='get',
               hdkey='beammajor')['value']
minor = imhead(imagename=myImage, mode='get',
               hdkey='beamminor')['value']
pixelSize = float(cell.split('arcsec')[0])
num = major*minor*np.pi
den = 4.0*np.log(2.0)
beamArea = (num/den)/(pixelSize**2)
peak = imstat(imagename=myImage)['max'][0]
thresh = peak/4.0

# loop over CLEAN making masks automatically until
# we hit our threshold
n = 0
while (thresh >= stop*rms):
    # make masks based on threshold
    autoMask = preName + '_autoMask' + str(n)
    # get values for masking as numpy arrays
    ia.open(myFlux)
    pbVals = ia.getchunk()
    ia.close()
    ia.open(myResidual)
    resVals = ia.getchunk()
```

```
cs = ia.coordsys()
ia.close()
if n == 0:
    mVals = np.zeros(resVals.shape)
else:
    ia.open(myMask)
    mVals = ia.getchunk()
    ia.close()
# create masking numpy array
nextMask = np.zeros(mVals.shape)
nextMask[resVals > thresh] = 1.0
nextMask[mVals > 0] = 1.0
nextMask[pbVals < minpb] = 0.0
# remove masking regions that are too small
labeled, j = sni.label(nextMask)
myHistogram = sni.measurements.histogram(labeled,
                                          0, j+1,
                                          j+1)
object_slices = sni.find_objects(labeled)
threshold = beamArea*beamMin
for i in range(j):
    if myHistogram[i+1] < threshold:
        nextMask[object_slices[i]] = 0.0
# save masking array as CASA, floats-only, image
im = ia.newimagefromshape(outfile=autoMask,
```

```
                        shape=list(nextMask.shape),
                            csys=cs.torecord())
    im.close()
    ia.open(autoMask)
    ia.putchunk(nextMask)
    ia.close()

    # clean with automatically generated mask
    if (thresh/2.0 < stop*rms
            and thresh < 1.05*stop*rms):
        restoringbeam = finalBeam
    else:
        restoringbeam = []
    os.system('rm -rf '+myMask)
    clean(vis=vis,
          imagename=preName,
          field=field,
          antenna=antenna,
          phasecenter=phasecenter,
          mode=mode,
          psfmode=psfmode,
          cell=cell,
          imsize=imsize,
          weighting=weighting,
          robust=robust,
```

```
            imagermode=imagermode,
            uvrange=uvrange,
            uvtaper=uvtaper,
            outertaper=outertaper,
            mask=autoMask,
            niter=10000,
            threshold=str(thresh)+'Jy/beam',
            restoringbeam=restoringbeam,
            cyclefactor=cyclefactor,
            minpb=minpb,
            interactive=False)
    thresh /= 2.0

    # if a little more than stopping threshold, run
    # with thresh=stop*rms
    if 2.0*thresh == stop*rms: break
    if (thresh < stop*rms
            and 2.0*thresh > 1.05*stop*rms):
        thresh = stop*rms
    n += 1

# go back to where we started
os.chdir(origDir)
```

Appendix C

Estimating Dust Properties

We needed estimates of the dust temperature, dust opacity per unit mass column density, and emissivity spectral index to calculate our dust-only maps and convert the dust flux densities to masses. Gordon et al. (2014) provide dust property maps of the entire LMC from three different dust SED models. We chose to use the broken emissivity modified blackbody (BEMBB) fit with the dust emissivity spectral index unconstrained because it gave the smallest residuals from their observations. This fit is to Herschel HERITAGE Key Project (Meixner et al. 2013) SED measurements across the LMC. Their dust surface brightness model starts from

$$S_\lambda = \kappa_\lambda \Sigma_\mathrm{d} B_\lambda(T_\mathrm{d}) \tag{C.1}$$

where S_λ is the dust surface brightness at a wavelength λ, κ_λ is again the dust opacity per unit mass column density, Σ_d is the dust mass surface density, B_λ is the Planck function, and T_d is the dust temperature. For the BEMBB they assume a single dust temperature and a blackbody modified by a broken

emissivity law. This means κ_λ from Equation 3.4 takes the form

$$\kappa_\lambda = \frac{\kappa^{\rm BE}_{\rm eff,160}}{160^{-\beta_{\rm eff,1}}} E(\lambda) \tag{C.2}$$

where $\kappa^{\rm BE}_{\rm eff,160}$ is the effective dust opacity at 160 µm for their broken emissivity model, $\beta_{\rm eff,1}$ is the effective dust emissivity spectral index below the emissivity break and $E(\lambda)$ is

$$E(\lambda) = \begin{cases} \lambda^{-\beta_{\rm eff,1}} & \lambda < \lambda_{\rm b} \\ (\lambda_{\rm b}^{\beta_{\rm eff,2}-\beta_{\rm eff,1}})\lambda^{-\beta_{\rm eff,2}} & \lambda \geq \lambda_{\rm b} \end{cases} \tag{C.3}$$

where $\beta_{\rm eff,2}$ is the effective dust emissivity spectral index above the emissivity break and $\lambda_{\rm b}$ is the wavelength at which the model emissivity switches from $\beta_{\rm eff,1}$ to $\beta_{\rm eff,2}$. This results in five free parameters for fitting their SEDs and so they provide maps for all five fit parameters across the LMC. It is from these maps that we measure the average dust temperature, the average dust emissivity spectral index corresponding to our observing wavelengths ($\beta_{\rm eff,2}$), and calculate the opacity from $\beta_{\rm eff,1}$, $\beta_{\rm eff,2}$ and $\lambda_{\rm b}$ for use in Equation 3.4.

While each field was resolved separately in the fit parameter maps, we averaged the parameters over 30 Dor-10, N159W, N159E and N113 because the individual averages of pixels covering each field separately were consistent within their uncertainties on the means. For example, the temperature pixels that covered 30 Dor-10 were averaged together and the uncertainty on the mean was calculated. This was repeated for each of the fields mentioned above and all of the field average temperatures were consistent within their uncertainties. Thus we chose to average all pixels across the four fields to

calculate the parameters needed for Equation 3.4.

Within their parameter maps from a single model are three additional options based on the method used for determining the best fit parameters. Given their fitting technique, they acquired a full posterior likelihood distribution for each of their fit parameters. This means there is not a single "correct" method to define a set of best fit parameters and so they provide three options. The first, which we chose to use for acquiring our dust parameters, is the maximum likelihood which is sometimes referred to as a "traditional χ^2" method. They found this estimate to be best suited for comparing fits to the observations and calculating residuals. We take this to mean that when that set of parameters is taken together, it best reproduces the observations and thus should be optimal for using the parameters together for deriving additional physical quantities, as we do here. Their other two methods were to calculate a likelihood weighted expectation value for each parameter from their posterior distributions or to randomly sample the parameter distributions to pick a realization of the full n-dimensional posterior. These should incorporate the individual parameter distributions' shapes and are described as being useful for large numbers of map pixels being treated in a statistical sense. As we are not working with a very large number of pixels from their maps, these second two methods did not appear optimal for our use.